 doi:10.20944/preprints202009.0738.v1

Eulerian and Lagrangian Comparison of Primary and Secondary Wind Jets in the Tokar Gap Region.

by

Larry J. Pratt[1], E. Jason Albright[2], Irina Rypina[1], Houshuo Jiang[1]

[1] Woods Hole Oceanographic Institution, Woods Hole, MA 02543

[2] Los Alamos National Laboratory, Los Alamos, NM 87545.

Correspondence: Larry J. Pratt (lpratt@whoi.edu)

 doi:10.20944/preprints202009.0738.v1

Abstract

The Lagrangian and Eulerian structure and dynamics of a strong wind event in the Tokar Gap region are described using a WRF model hindcast for 2008. Winds in the Tokar Gap reach 25 m s^{-1} and remain coherent as a jet far out over the Red Sea, whereas equally strong wind jets occurring in neighboring gaps are attenuated abruptly by a jump-like hydraulic transition that occur just offshore of the Sudan coast. The transition is made possible by the supercritical nature of the jets, which are fed by air that spills down from passes at relatively high elevation. By contrast, the spilling flow in the ravine-like Tokar Gap does not become substantially supercritical and therefore does not undergo a jump, and also carries more total horizontal momentum. The Tokar Wind Jet carries some air parcels across the Red Sea and into Saudi Arabia, whereas air parcel trajectories in the neighboring jets ascend as they cross through the jumps, then veer sharply to the southeast and do not cross the Red Sea. The mountain parameter Nh/U is estimated to lie in the rage 1.0-4.0 for the general region, a result roughly consistent with a primary gap jet having a long extension, and supercritical jets spilling down from higher elevation passes. The strong event is marked by the formation of a cyclonic cell near the upstream entrance to the Tokar Gap, a feature absent from the more moderate events that occur throughout the summer. The cell contains descending air parcels that are fed into the primary and secondary jets. An analysis of the Bernoulli function along air parcel trajectories reveals an approximate balance between the loss of potential energy and gain of internal energy and pressure, with surprisingly little contribution from kinetic energy, along the path of the descending flow. All jets attain the critical wind

 doi:10.20944/preprints202009.0738.v1

speed nominally required to loft dust into the atmosphere, though only the Tokar Gap has a broad, delta region with plentiful deposits of silt.

1. Introduction

The Red Sea is fringed along much of its coastline by low mountains, including the Asir Range in Saudi Arabia and the Red Sea Hills in the northeastern Sudan, all of which are thought to channel the prevailing winds along the axis of the Red Sea (e.g. Patzert 1974). However, both ranges are punctuated by gaps and passes, and these have been linked to strong, localized offshore wind jets and funneled onshore winds (Jiang et al. 2009 and references therein). The best-known example of an offshore jet occurs in the summer, when the southwest monsoon blows through Sudan's Tokar Gap (Fig. 1a). The Tokar Wind Jet (hereafter TWJ) achieves wind speeds upwards of 25 m s^{-1} and is associated with summer dust storms (Fig. 2) and enhanced localized surfaces stresses and eddy generation in the Red Sea (Zhai and Bower 2013). Based on a 30-year wind/wave climatology, Langodin et al (2017) concluded that the highest surface waves in summer are generated at the center of the Red Sea and are a consequence of the TWJ. Observations and model results (Viste and Sorteberg 2011; Davis et al. 2015) suggest that the Tokar Gap is part of an inland conduit for Indian Ocean monsoons, delivering a significant summer source of atmospheric moisture to the southern Red Sea and thence to the East African Highlands.

 doi:10.20944/preprints202009.0738.v1

Model simulations indicate the presence of other wind jets that form in gaps in the Red Sea Hills and Asir Mountain Range (Jiang et al., 2009; Davis et al. 2020). We are primarily concerned with summer winds that form in the Tokar Gap and neighboring gaps, especially two unnamed gaps to the south (labeled Gap 2 and Gap 3 in Fig 1a). Although the wind speeds in some of these gaps reach or exceed the 25 m/s seen in the TWJ, the associated wind jets do not have nearly the same downstream reach as the TWJ. This difference is relevant to local climate in that the monsoon moisture carried northeastward by the secondary jets does not penetrate all the way across the Red Sea and into Saudi Arabia.

Gap winds occur when air is driven from high to low pressure through the passes or cols in a mountain ridge. The funneling effect can produce low-level jets that extend well downstream of the ridge, an effect that can be enhanced in coastal areas due to the reduced drag coefficient over water. Coastal gap winds contribute significantly to local circulation patterns, extreme weather events, atmospheric transport, and the generation of ocean eddies. Sites of prominent gap winds in coastal regions include the Strait of Juan de Fuca (Reed 1931; Overland and Walter 1981; Colle and Mass 2000), the Gulfs of Tehauntepec and Papagayo (Clarke 1988; Steenburgh et al. 1998; Chelton et al. 2000), the Columbia River Gorge (Sharp and Mass 2004), the Dinaric Alps (Gohm et al. 2008) and the straits and gaps in the Philippine Archipelago (Pullin et al. 2003; Rypina et al. 2010). There are also many non-coastal examples (e.g. Mayr et al. 2007). Sun and Yu (2006) suggest that eddies spun up by the Tehuantepec gap winds can influence the annual cycle of sea surface temperature (SST) in the eastern Pacific warm pool. Rypina et

 doi:10.20944/preprints202009.0738.v1

al. 2010 show that ocean dipoles spun up by gap winds in the Philippine Archipelago can strip nutrient-laden waters from the coast and transport the nutrients far offshore.

The driving of air from high pressure to low pressure across the Red Sea Hills is evident in a regional simulation (Fig.3) using the Weather Research and Forecasting (WRF) model, the model used in this study. Within the topographic gaps, the 10 m winds (red arrows) cut across the (blue) contours of constant sea level pressure. The fields shown are means for July 2008 and the wind jets that form are not as distinct as they would be in instantaneous examples (e.g. Fig. 8 below) but the mean TWJ can clearly be seen near 18^{o}N and the mean expressions of several other gap flows can be seen to the south. Fig. 1 also shows some topographic characteristics that set the Tokar Gap (TWJ) apart from other gaps in the region. To begin with, the topography is more typical of ravine than a mountain pass or col, with elevations dropping approximately 500 m from the interior Sudanese plateau to the Tokar Delta over a distance of about 400 km. Peaks to the immediate north and south of the Tokar Gap lie at 1000↓1500m elevations. By contrast, Gaps 2 and 3 contain topographic passes or cols at 1360 m and 1430 m elevation and these potentially block lower level flow. At the head of the Tokar Gap lie two tributary canyons (hereafter the north and south entrance channels) that merge to form the main canyon (Fig. 1). The gap then descends through its narrowest width of about 100 km before reaching the Tokar Delta, a rich alluvial plain formed by flooding of the Baraka River and extending 50 km to the Red Sea and 80 km in either direction along the coastline. Both the Arabian and African coasts are sources of silt for dust storms (Kalenderski and Stenchikov 2016). Hickey and Goudie (2007) have identified the

 doi:10.20944/preprints202009.0738.v1

Sudanese coast immediately around the Tokar Gap delta as one of two major sources regions for silt for Northern Hemispheric dust storms (Fig. 2). By contrast, Gaps 2 and 3 terminate closer to the coast and do not have broad deltas.

A feature that distinguishes the TWJ and neighboring gap jets from many other coastal gap winds is their strong diurnal variability. Jiang et al. (2009) found that the jets are present on a nearly daily basis from mid-June thru mid-September in a 2008 hindcast. There is a strong daily cycle, with winds typically peaking around 04-06 UTC (7–9 AM local time) and maintaining a high directional consistency. The Red Sea also experiences a strong land/sea breeze (Pedgley 1974), but the phasing can be slightly different from that of the TWJ. Davis et al. (2015) cite the diurnal variation of the intertropical discontinuity, the leading edge of the southern monsoon air mass that feeds the TWJ, as a possible influence. The elevated moisture content of the jets constitutes another distinguishing feature. During the week-long simulation analyzed by Davis et al. (2015) the elevated humidity levels in the TWJ and neighboring jets led to significant pulses of moisture into the southern Red Sea region.

Our primary purpose is to compare and contrast the downstream reach of the TWJ and secondary jets, and to identify key dynamical processes that account for the differences. Included in the analysis will be maps of air parcel pathways at different levels for the three jets as a way to provide comparison in terms of upstream origins and downstream destinations. This Lagrangian analysis also allows for quantification of the energy transformations that occur along pathways. To set the stage for these analyses we present

 doi:10.20944/preprints202009.0738.v1

information regarding the overall Eulerian structure, time dependence, and hydraulic transitions characteristic of a wind event that occurred on 11-12 July 2008 and that is the central focus of our paper. The analysis is done using the same regional model output that was analyzed by Davis et al. (2005). A key element that will emerge is that the vertical thickness of the jets in the neighboring gaps is less than that of TWJ, whereas the peak winds are at least as large, causing them to be hydraulically supercritical and therefore subject to hydraulic jump formation. These features are described in Section 3 along with other relevant properties. Differences in Eulerian properties also lead to differences in Lagrangian characteristics, in terms of the rate of stirring of air parcels, in the energy conversions that take place along parcel trajectories, and in the geographic origins and destinations of parcels, all discussed in Section 4. Section 5 briefly explores some related issues, including comparison with other strong wind events in the region and conditions for lofting dust into the atmosphere.

2. Model Overview

Our results are based on 14-month run of the Weather Research and Forecasting (WRF) model, version 3.0.1.1, with a 10-km horizontal resolution Red Sea subdomain nested within a 30-km resolution domain covering most of the Middle East, for which the 1° NCEP Global Final Analysis was used as initial and boundary conditions. The model employs 35 vertical levels, uses terrain-following eta coordinates, has daily reinitializations, and produces output at 1 hour intervals. Further details can be found in Skamarock et al. (2008) and Lo et al. (2008). The model run was originally produced by

 doi:10.20944/preprints202009.0738.v1

Jiang et al. (2009), who describe validation based on surface wind speed from an air/sea buoy moored of the Saudi coast (Farrar et al. 2009). Further validation is described by Davis et al. (2015) who compared model output with radiosonde soundings of temperature, wind speed and water vapor at six observation stations located in Saudi Arabia and Egypt. Comparisons with vertically smoothed profiles were generally found to be good. A caveat is that the authors were unable to find *in situ* data within the Tokar Gap, or along the neighboring Sudan coast. For more details on the model validation, the reader is referred to Davis et al. (2015).

3. Eulerian Structure.

a. Diurnal Variability

Jiang (2009) and Davis (2015) have documented the strong diurnal character of the gap winds, which typically begin around 00 UTC (3 AM local time) and terminate around 12 UTC. The strongest wind event in the 2008 WRF model hindcast began late at night on 11 July and continued through the morning and into the early afternoon of 12 July. We now consider the temporal, structural and dynamical aspects of the TWJ (also referred to as the “primary jet” wind jet), along with the winds in Gaps 2 and 3 (also referred to as the “secondary jets”), during this time period. The three-dimensional structure and evolution of the primary and secondary jets are revealed through data plotted at the stations and along the section lines indicated in Fig. 1.

 doi:10.20944/preprints202009.0738.v1

A view of the temporal evolution of the wind field over the 24-hour period of 12 July 2008 is provided by Hovmöller plots showing the horizontal velocity as a function of elevation and time (Fig. 4). The three plots are made at successive locations proceeding downstream: near the upstream entrance of the Tokar Gap (Fig. 4a), in the narrowest part of the Tokar Gap (4b), and out over the Red Sea (4c). All locations are indicated by stars in Fig. 1 and each was selected to lie in the high velocity core of the flow. The velocity contours indicate the magnitude of horizontal velocity directed along the axis (or 'thalweg') BCDE that begins in the north entrance channel of the Gap.

The evolution below 2000 m shows a strong diurnal character, with high velocities during the night and early morning and nearly stagnant conditions during the late afternoon. The down-canyon winds extend up 1500↓2000 m above ground level and are generally weakest near the channel entrance, strongest at the narrowest section (Fig. 4b), and still strong at the Red Sea section (Fig. 4c). The downslope winds relax at around 12 UTC but remain positive in the gap itself. At the Red Sea location the surface winds are eventually overcome by the opposing sea breeze and reverse direction at about 14 UTC. It is notable that the velocities in Fig. 4c, which are predicted at a location nearly midway across the Red Sea, are nearly as large as those in the narrows (Fig. 4b). A striking feature of all plots is the reverse flow that develops aloft, roughly between 1500 m and 3500 m, and is strongest when the jet is active. Gohm et al. (2008, Figs. 5c and 5f) notice a similar wind reversal during the strong phase of a bora.

 doi:10.20944/preprints202009.0738.v1

b. longitudinal structure

Insights into the along-axis thermal and velocity structure of the Tokar Gap flow can be gained from the Fig. 5a,b plots of potential temperature and along-axis velocity along the piecewise constant paths ADE and BCDE. The plots show data at 05 UTC, corresponding to peak winds in the downstream reaches of the gap. The overall longitudinal picture is one of spilling and acceleration through the compound gap, with the highest velocities of approximately 20 m/s occurring downstream of the junction (D), where the gap narrows and then opens up over the delta. There is also some evidence of a decrease in static stability above the outflow: for example, the vertical displacement between the 315 K and 318 K potential temperature surfaces increases from 1000 m to 2000 m in the downstream direction. Another notable feature in the thermal structure is a slight increase in ground level potential temperature where the winds descend over land, followed by a decrease where the winds blow out over the cooler Red Sea.

Comparison with the winds in Gap 2, plotted at 05 UTC in Fig. 6, reveals larger peak winds (≅25m/s) along the downslope, and in the region extending from the pass near 80 km to the Red Sea shoreline near 165 km. However, the strong winds terminate about 10 km offshore. Whether one takes the 312 K or 315 K potential temperature contour as an upper boundary for the descending flow, the vertical thickness (700-1000 m at the 125 km mark) is somewhat smaller than the thickness of the downslope wind layer in the Tokar Gap. The 312 K surface rises abruptly downstream of the core of strongest

 doi:10.20944/preprints202009.0738.v1

downslope winds, whereas the same surface continues to descend (Fig. 5) where the Tokar Gap winds run out over the Red Sea.

c. Three Dimensional Structure

For gap wind applications, the branching, ravine-like topography of the Tokar Gap is less typical than the topographies of Gaps 2 and 3. For this reason, we examine the three-dimensional structure of the Tokar Gap winds further using a series of cross-sections (Figs. 7a↓g), plotted at 05 UTC and proceeding from upstream to downstream. Each section shows potential temperature and the normal component of horizontal velocity, with the viewer facing downstream. The section composited from *aa′*, *a′a″*, and *a″a‴* (Fig. 7a) lies upstream and crosses both approach channels. Separate cores of moderately high velocity, with values up to 15 m s^{-1}, can be seen on either side of the small ridge (near 10 km in the right-hand panel) that separates the channels. At section *bb'* (Fig. 6b), which is located at the junction of the approach channels, the separate jets merge to form a single core. The section extends to the north and south (left and right) across the bounding ridges. A high-speed core of flow can be seen along the sloping terrain to the south, across the ridge located near 200 km, revealing the presence of strong winds in this neighboring gap. Section *cc′* (Fig. 7c), which cuts across the narrowest part of the gap, shows even higher velocities concentrated in a single core that fills the primary gap but continues into the neighboring gap to the south. Section *dd′* cuts across the delta, *ee′* lies near the shoreline, and *ff′* and *gg′* lie mostly offshore (Figs. 7d↓g). The narrow (150 km wide), high velocity (25 m s^{-1}) core continues through *ff′*,

 doi:10.20944/preprints202009.0738.v1

diminishing somewhat by *gg′*. At section *ee′* there are shallower, secondary regions of high velocity to the left and right (north and south) of the primary core. In the region lying between 0 and 100 km in Fig. 7e the high winds are due to air spilling down the slope of the ridge that lies immediately to the north of the Tokar Gap. The weaker core to the south (between 300 and 350 km) consists of flow from Gap 2, which lies to the south of the Tokar Gap.

The surface expression of all three jets (Tokar, Gap 2 and Gap 3) during maximum intensity (05 UTC) are apparent in maps of 10 m winds (Fig. 8a) and surface potential temperature (Fig. 8b). Secondary jets and the neighboring downslope winds experience an increase of surface potential temperature as they spill down over land, then undergo a decrease in potential temperature as they leave the coast and move offshore. By contrast, the TWJ experiences only very little offshore cooling. The disproportionally large reach of the TWJ compared to secondary jets during this event is apparent in Fig. 8a but it is not explained by differences in the surface winds, since the maximum speeds in the (narrower) secondary jets are as large as those in the TWJ.

d. Mountain Parameter

There have been a number of modeling studies of gap winds in idealized settings, including Overland (1984), Saito (1993), Zangl (2002), and Gabersek and Durran (2004 and 2006). Gabersek and Durran (2004), consider a long ridge of height h and an upstream wind with uniform velocity U and buoyancy frequency N, approaching from the

 doi:10.20944/preprints202009.0738.v1

direction perpendicular to the ridge. A notch is cut through the ridge and thus an approaching air parcel can go around or over the ridge, or through the gap. The lowest elevation in the gap is the same as that of the surrounding flat terrain, so there is no sill.

One of the key parameters for flow over ridges with or without gaps is *Nh/U*. For values less than about 0.5, the flow tends to be inertial and the lower level air parcels ride directly up and over the topography in the manner of a hydraulically supercritical flow. For this regime, there is little tendency in the Gabersek and Durran (2004) model for the flow to divert around the ridge or through the gap, and consequently a strong jet does not form in the gap. When *Nh/U* exceeds a critical value, generally in the range 0.7↓1.1 for a ridge without a gap, breaking internal gravity waves begin to appear in the lee of the ridge crest (Baines 1995). The turbulence so generated can lead to the formation of a mixed layer or wedge of homogenized and relatively stagnant air. The wedge acts as a reflecting upper boundary for the flow below, which may then behave as a finite-depth layer that can undergo hydraulic transitions. Gabersek and Durran (2004) observe this behavior in experiments with *Nh/U* values of 1.4 and 2.8. There, breaking internal waves are observed in the lee of the ridge crest, away from the gap, and underneath these waves is downslope flow that terminates in a feature resembling a hydraulic jump. Downstream of the jump the winds diminish considerably and a wake forms. A strong jet forms within the gap itself and this jet continues as a concentrated, narrow flow well downstream of the ridge. Slow, wake-like circulations consisting of counter-rotating gyres form on either side of the jet. When *Nh/U* is increased to the value 5.0, there is an even greater tendency for the flow to be blocked by the ridge and much of it goes around.

There is decreased flow into the gap and over the ridge top, and the strength and extent of the gap jet are diminished.

Estimation of *Nh/U* for the Tokar Gap /Red Sea Hills region is difficult due to the nonuniformity of the upstream winds and the complexity of the topography. As shown in Fig. 1a, much of the terrain upstream of the gap (lower left portion of Fig. 1a) consists of a broad plain lying at about 400 m elevation. The elevation of the ridges and peaks that border the Tokar Gap ranges from 1200↓2000 m, so reasonable range of *h* is 800↓1600, and we will use the average value 1200 m. Wind profiles (Fig. 9) taken at three locations within the upstream region at 00 UTC show winds directed towards northeast (towards the gap) up to about 750 hPa (or about 2500 m) above terrain, above which they reverse direction. The average wind speed over this range is 6↓8ms^{-1}. The corresponding profiles of buoyancy frequency N [$=g\theta^{-1}d\theta/dz$] have value (.012±.002) s^{-1} over much of this range, but decrease to zero near ground (Fig. 9). We average these values from ground level to 750hPa in order to estimate the scales *U* and *N*. The resulting estimate of *Nh/U*, computed over the duration of the strong wind event (roughly 10 UTC on 11 July to 15 UTC on 12 July) varies from between 1.0 and 4.0. For the model considered by Gabersek and Durran (2004), such values would suggest the existence of a strong gap jet with a long downstream extension as well as spilling flows across higher elevation ridges. However, the ridge in the Gabersek and Durran (2004) model lies at constant elevation, whereas the Red Sea Hills ridges are irregular and punctuated by peaks and cols, so there is little guidance as to where exactly spilling and lee wave breaking would occur. Also, there is no evidence of the weakly recirculating or

 doi:10.20944/preprints202009.0738.v1

stagnant ‘wake’ eddies that are seen in Gabersek and Durran (2004), possibly because the multiple jets in our case are too closely spaced to allow such features between them. The presence of the prevailing northwesterly winds along the axis of the Red Sea may also discourage closed circulation patterns.

e. Downstream turning

Hickey and Goudie (2007) refer to the anticyclonic bending of dust plumes emanating from the Tokar Gap. As a result, the dust is transported southeast, along the axis of the Red Sea, sometimes covering the entire southern portion. This picture is consistent with the behavior of the 10 m winds (Fig. 8a,b), which show the TWJ extending across the Red Sea towards the Saudi coast and then veering towards the southeast. The veering is even more pronounced for the secondary jets, although they do not extend as far offshore. The inertial radius U/f based on a typical velocity U=15 m s^{-1} at 20°N is about 300 km, which is only moderately larger than the 200 km radius of curvature required for a southwesterly wind to veer anticyclonically 90° and flow towards the southeast before reaching the Saudi coast. So the idea, mentioned by Hickey and Goudie (2007) and others, that the turning is simply due to the Coriolis acceleration acting on the jets, has some support. However, bending may also be induced by collision of the TWJ with the prevailing, geostrophic northwesterly winds that flow along the axis of the Red Sea. We also note that the Rossby number U/fL for a L=150 km wide jet with the above velocity scale is about 2, so the inertial character of the jets is significant.

 doi:10.20944/preprints202009.0738.v1

f. abrupt transitions

In order to interpret some of the behavior cited above, it is helpful to make an analogy with the hydraulics of a single, homogeneous layer flowing beneath an inactive upper layer. The shallow-water analogy has been used in connection with other spilling mountain winds (e.g. Gohm et al. 2008). Baines (1995) describes a number of conditions that would allow shallow-water/hydraulic interpretation to be valid. These include the presence of wave overturning aloft, which can produce a reflecting upper boundary, and the presence of a reflecting critical level. The features are certainly not ubiquitous in our model runs, but there is evidence of their presence at certain times and locations. For example, the wind reversals observed above the jet indicates that the along-axis flow changes sign at a level slightly above that of the spilling layer/jet (Figs. 4-7). This level would also correspond to a critical level for stationary disturbances. In addition, the TWJ and secondary jets, though stratified, exhibit strong vertical coherence, as would a single, homogeneous layer.

As a bounding upper surface or interface of this hypothetical layer, we pick an isentropic surface (here 312 K) that roughly marks the top of the range of high, down-slope velocities. Inspection of Fig. 5 suggests that the 312 K surface is a reasonable choice, particularly over the high-velocity portions of the downstream flow. The resulting lower layer thickness (Fig. 10a) suggests a pattern of spilling and thinning as air travels through the Tokar and secondary gaps and out over the Red Sea. A significant difference is that the secondary flows (including the downslope flows in Gaps 2 and 3, and along the

Preprints (www.preprints.org) | NOT PEER-REVIEWED | Posted: 30 September 2020 doi:10.20944/preprints202009.0738.v1

neighboring terrain), which contain air spilling from higher elevations, become quite shallow (dark blue) over the sloping terrain, but experience a rebound in layer thickness (light blue) as they move out over water. In contrast, the Tokar Gap outflow thins continuously as it spills out over the Red Sea, though it never becomes as shallow as the secondary jets. Note that the spilling air is not confined to the main and secondary jets, but occurs broadly over the downslopes, as suggested in Fig. 8a,b.

The local hydraulic state of the active layer of a 1.5-layer system is measured by the local Froude number

$$F_d = \frac{U}{(g' d)^{1/2}},$$

where g' is the reduced gravity $g(\bar{q}_2 - \bar{q}_1)/\bar{q}_1$ based on the average potential temperatures $\bar{q}_1$ and $\bar{q}_2$ below the interface and in the region of homogeneous potential temperature above the interface. Also, $U = (\bar{u}^2 + \bar{v}^2)^{1/2}$ is the magnitude of the average horizontal velocity $(\bar{u}, \bar{v})$ over the layer. A plot (Fig. 10b) of F_d for the entire region, taken near peak wind conditions, suggests that the TWJ does not undergo any significant hydraulic transition as the jet leaves the Gap. The Froude number of the exiting flow is close to unity and remains roughly so as the jet crosses the 200 km breadth of the Red Sea (green area).

 doi:10.20944/preprints202009.0738.v1

Significant hydraulic transitions are indicated near the base of the Red Sea Hills within the secondary jets and neighboring downslope flows, where F_d reaches values that approach 5.0. An example is the jet that forms in Gap 2 immediately to the south of the TWJ and that spills from a pass of elevation 1360 m lying between two peaks of above 1500 m. As shown by a longitudinal section of this flow (Fig. 6), the overlying 315K contour descends down the lee slope but suddenly rises at the base of the slope (near 150 km). For a single layer flow, the relative change in layer thickness across a jump is given by

$$\frac{d_1}{d_o} = \frac{\sqrt{1 + 8F_o^2} - 1}{2}, \qquad (1)$$

where F_o is the value of F_d just upstream of the jump and d_0 and d_1 are the values of layer thickness just upstream and downstream of the jump (e.g. Pratt and Whitehead 2008). This formula expresses the general tendency for relative change d_1/d_0 to become larger as the upstream Froude number increases, but it ignores features such as bottom friction, entrainment and continuous stratification. With F_o and corresponding d_o values that range between (2.5, 250 m)–(5.0,100 m) for the secondary flows to the south of the Tokar Gap (Figs 10a,b), the predicted downstream thickness d_1 is 650–770 m. The downstream thickness values apparent in Fig. 10a (light blue to light green) lie in the range 700–1000m. It is therefore reasonable to conclude that observed transitions have some

Preprints (www.preprints.org) | NOT PEER-REVIEWED | Posted: 30 September 2020 doi:10.20944/preprints202009.0738.v1

similarity to classical hydraulic jumps, though this assertion comes with the caveat that the WRF model resolution may be insufficient to capture rotors and other detailed structures observed downslope wind transitions (e.g. Gohm et al. 2008).

g. downstream extent

The presence of hydraulic transitions in the secondary jets, and the absence of such in the Tokar Wind Jet, suggests that the latter might have much longer downstream extent than the former, as observed. For one thing, the TWJ would not suffer the energy dissipation that occurs in a hydraulic jump, and that is proportional to the cube of the upstream/downstream difference in layer thickness. Another quantity that favors the TWJ in terms of downstream reach is the offshore momentum flux. For a 1.5-layer system, the momentum flux (or total 'flow force') per unit breadth is given by

$$M = g\rho d^2 + \bar{u}^2 d$$

where $\bar{u}$ is the offshore component of the vertically averaged velocity over the layer. With estimated values of the layer thickness d and velocity along the centerlines of the TWJ and Gap 2 jet, we find M in the range $(6–10)\times10^5$ m^2 s^{-1} for the former, and $(2–3)\times10^5$ m^2 s^{-1} for the later. So despite the fact that the offshore velocities in the secondary jets can be larger than those in the TWJ, the latter carries two to three times larger total momentum flux than the secondary jets.

 doi:10.20944/preprints202009.0738.v1

4. Lagrangian Structure

To obtain a more comprehensive view of the Lagrangian structure of the winds in and around the Tokar Gap, we initiate groups of trajectories in the high-speed outflow regions and integrate backward and forward in time. For example, Fig. 11 shows backward-time (red) and forward-time (black) trajectories initiated at 100 m elevation and within a small horizontal region lying close to where the TWJ crosses the coast. (The region is formally defined as that where the wind speed exceeds a threshold value, here 15 m s^{-1}.) The trajectories are integrated from the initiation time (also labeled on each frame) backward to 12 UTC on the previous day (11 August 2008), and forward to 24 UTC of the current day (12 August 2008), thus revealing information about upstream sources and downstream extent of the wind event. Frames a-d, which show the results of releases at 00, 03, 06 and 09 UTC, suggest that while some of the flow is fed upstream by low-level winds over the plateau to the southwest of the Tokar Gap, there is also a significant contribution from an isolated cell of descending air parcels. Comparison of Frames b, c, and d indicate that this cell is slowly moving upstream, seen more clearly in a video (see WRFVEL_0711 in Supplemental Information). As for the downstream (black) segments, it is apparent that the majority of air parcels cross the Red Sea and come close to the Saudi coast, some penetrating inshore and up and over the Saudi coastal mountain range (Frame a). This penetration is notable given the excess moisture content of such parcels, as described by Davis et al. (2015).

 doi:10.20944/preprints202009.0738.v1

A better view of the vertical Lagrangian structure of the TWJ appears in Fig. 12, where the viewer now faces southeast. Each frame shows four groups of color coded trajectories initiated at levels of 100m, 500m, 1000m and 1500m, and the release times are as in Fig. 11. It can be seen that the funneling winds are fed by a horizontally broad collection of trajectories that cover the upstream plane. Trajectories released at higher levels, colored yellow, tend to originate from the north portion of the upstream plateau (the portion closer to the viewer). Interestingly, trajectories released at lower elevations (magenta) predominantly originate from the southern portion of the plateau and make up the bulk of the air parcels that descend from the isolated cell mentioned in the previous paragraph. A small number of the trajectories originate at higher elevation above the Red Sea and move westwards before descending and reversing direction as they flow down into the gap. The forward (green and blue) trajectories all cross the Red Sea, and most of the ones released at lower elevation (predominantly blue) cross the Saudi coast and penetrate inland.

The wind jets that form in Gap 2 and Gap 3, exhibit some Lagrangian characteristics that are distinct from those of the TWJ. The winds in Gap 2 spill over a relatively high and narrow sill at 1360 m elevation (Fig. 6). Trajectories initiated within the outflow region at 100 m (not shown) show no connection to the upstream cyclonic cell, while those initiated at (or above) 500 m (Fig. 13a-d) exhibit a strong connection. In addition, none of the trajectories cross the Red Sea but instead turn southwards and flow parallel to the coast, some eventually crossing back into Africa (frames a-c). A magnified and rotated view (Fig. 13e) of Frame c more clearly shows that after air parcels leave the coast, they experience a rapid ascent as they pass through the suspected hydraulic jump, then turn

 doi:10.20944/preprints202009.0738.v1

rapidly towards the southeast. Trajectories in Gap 3 (not shown), which is broader than Gap 2 and has a higher-elevation (1430 m) sill, exhibits similar features.

The upstream region of descending air parcels bears resemblance to a feature identified by Davis et al. (2015) in connection with a separate strong wind event in the Tokar Gap (see the 'downburst' in their Fig. 9c). The event in question began during the late evening of 8/12 and extended into 8/13. Videos of the two events (see WRFVel_0711 and WRFVel_0712 in Supplemental Information) reveal that in both cases the feature is a cyclonic cell that forms near the upstream entrance to the Tokar Gap at about the same time as the gap winds begin to blow. The videos also show that the feature propagates upstream (westward), and eventually out of the high-resolution subdomain. The northern edge of the monsoon air mass is also aligned in the east-west direction and the cell follows this edge as it moves to the west.

The connection between the cyclonic cell and the jet outflows is further illustrated in Fig. 14, where trajectories are initiated at 1000 m (Frames a-c) or 1500 m (Frames d-f) and within the core of the cell (defined as the horizontal area in which the downward velocity exceeds 0.25 m s^{-1}). Backward-time (red) segments show that some of the air parcels descend from as high as 3000↓4000 m, while others can be traced upstream along more horizontal paths. The upstream drift of the cell as a whole is also apparent over the elapsed time of 6 hr. The forward-time (black) segments all pass downstream through

Preprints (www.preprints.org) | NOT PEER-REVIEWED | Posted: 30 September 2020 doi:10.20944/preprints202009.0738.v1

the Tokar Gap proper when initiated at 1000 m, while some trajectories initiated at 1500 m enter the Gaps 2 and 3.

Energy transformations experienced by air parcels along the paths of the jets are revealed by an examination of the terms that compose the Bernoulli function *B* for compressible flow (Kundu and Cohen 2008):

$$B = e + \frac{p}{r} + \frac{|\mathbf{u}|^2}{2} + gz = c_v T + \frac{p}{r} + \frac{|\mathbf{u}|^2}{2} + gz \qquad (2)$$

where *e* is the specific internal energy. For a dry gas, the latter is equal to the product of the specific heat c_v [assumed to have constant value 171 J/(kg K)] and the *in situ* temperature *T*. In a steady, adiabatic and isentropic flow, *B* is conserved along fluid trajectories. While these conditions do not generally hold in our applications, the winds during the strong phase of the 12 July 2008 event are approximately steady and, as we will show, the value of *B* undergoes only slight variation for an air parcel descending through the Tokar Gap or neighboring gaps during this phase of the event. In addition, the variation of *B* during this phase can be shown to be primarily due to diabatic heating.

We have chosen 5 trajectories (Fig. 15f) along which to track changes in B and its constituents. Two of the trajectories pass through the Tokar Gap and three pass through Gap 2. The former are colored pink upstream of, and green downstream of, the release locations (blue dots) near the coast. The trajectories passing through Gap 2 are colored

 doi:10.20944/preprints202009.0738.v1

red/black. The time histories of *B* and its constituents for each trajectory are tracked in the left-hand panels of Fig. 15.

For all trajectories, *B* experiences only small and gradual changes (Fig. 15*a*) during the 8-hr period before release and the 4-hr period after release, which covers most of the duration of the event. However, each experiences an abrupt increase in *B* right around the release time at t=18 (06 UTC, or 09 LST). At this time, the five air parcels have descended to the coastal plain and are about to move out over the water. The increase in *B* can be attributed to diabatic heating, as evidenced by an increase in potential temperature (Fig. 15*g*). In fact, changes in *B* over the entire period track potential temperate changes closely, suggesting that it is diabatic heating/cooling, and not time-dependence, that is primarily responsible for changes in *B*.

The plot of potential energy *gz* (Fig. 15*d*) shows that the Tokar Gap trajectories (in pink) experience a gradual and nearly monotonic descent as they pass through the gap and out over water during the first 6 hours of the stong wind event, whereas the Gap-2 trajectories (in red) ascend and then descend rapidly as they move up and over a ridge at much higher elevation. The Gap-2 trajectories also experience an abrupt rebound (at about t=8) shortly after they have moved out over water (see black extensions of red curves). This rebound coincides with the suspected hydraulic jump. Panel *e* shows that the kinetic energy of the air parcels in the Tokar Gap outflow remains high for 3 or 4 hours after the parcels have left the coast, whereas the Gap-2 trajectories experience a sudden decrease

 doi:10.20944/preprints202009.0738.v1

in kinetic energy at the positions of the jumps. Although the changes in kinetic and potential energy meet expectations for a hydraulic jump, the value of *B* itself does not experience any notable change. As shown in Frame *g*, the jump occurs during the period when the air parcels are experiencing the strongest periods of diabatic warming, and this may compensate for the dissipation of kinetic energy within the jump (a process that is poorly resolved by the model). We also note that Ogden and Helfrich (2016) have documented examples of stratified jumps that exhibit little or no energy dissipation. A model with higher horizontal and vertical resolution may ultimately be needed to clarify this picture.

Overall, the most significant constituents of *B* are the pressure term p/ρ, the potential energy gz and the internal energy $c_v T$ (Fig. 15, panels *b*-d). As the air parcels descend over the topography, $c_v T$ and p/ρ both increase at the expense of gz. Interestingly, although the kinetic energy increases it does not contribute significantly to the balance. This is in sharp contrast to deep overflows in the ocean (Pratt and Whitehead 2008), which are nearly incompressible and experience only minor changes in internal energy, and where the kinetic energy increase plays a more substantial role in the overall budget.

Although the flow in Gaps 2 and 3 likely experience hydraulic jumps, the overall horizontal spread of air parcels is weaker than for the TWJ. To quantify particle spreading, we computed the single-particle dispersion tensor $D_{ij} = \frac{1}{N}\sum_{n=1}^{N}\left(dx_i^n - \overline{dx_i}\right)\left(dx_j^n - \overline{dx_j}\right)$

Preprints (www.preprints.org) | NOT PEER-REVIEWED | Posted: 30 September 2020 doi:10.20944/preprints202009.0738.v1

where $i, j = 1,2,3$ correspond to the Cartesian coordinates x,y,z, overbars denote the ensemble mean, and $dx_i^n = x_i^n(t) - x_i^n(0)$ is the displacement of an n-th parcel from its initial position. The dispersion matrix can then be put in a diagonal form, with the 3 eigenvalues, D_τ, D_n, D_z, on the diagonal. A comparison (Fig. 16) based on these three coefficients between trajectories released at the exits of the Tokar Gap (left panels) and Gap 2 (right panels) yields some striking differences. At each location, a group of 25 air parcels is released every hour from 00 UTC until 09 UTC at z=500 *m* elevation at the exit and where velocity exceeds 15 m/s. The horizontal components of dispersion, D_τ and D_n for trajectories released in Gap 2 grow at a slower rate than those for an equivalent group of parcels released at the exit of the Tokar Gap. The difference is not surprising given the large spread of trajectories originating in the Tokar Gap (top panels of Fig. 16). The vertical dispersion D_z, on the other hand, is slightly larger for the Gap-2 parcels during the initial 6 hours since particle release and until TWJ parcels reach the opposite coast and start rising up over the mountain ranges, at which time the vertical dispersion for the TWJ parcels becomes larger. The same is true for parcels released at 100 m (not shown). In both cases the dispersion is dominated by the horizontal spreading of the trajectories, which is more pronounced in the TWJ.

5. Discussion

The strong wind event discussed in this paper exhibits structural similarities with several other strong wind events during July and August (not shown) in the WRF model. Peak

 doi:10.20944/preprints202009.0738.v1

winds in the Tokar Gap during those events are 20 m s^{-1} or less, and although the wind jets extend far out over the Red Sea, they exhibit stronger veering to the southeast and do not always reach the Saudi coast. The increased veering is consistent with a decreased inertial radius U/f and also with a greater influence of the ambient northwesterly winds blowing along the axis of the Red Sea. During the other events, the layer thicknesses based on the 312 K surface are generally smaller than during our 12-August-2008 extreme event , and the local Froude number distributions shows marginally supercritical flow within the Tokar Gap and supercritical flow within Gaps 2 and 3. As in the extreme case on 12 August 2008, the jets in Gaps 2 and 3 experience an increase in layer thickness and drop in speed, possibly due to hydraulic jumps, as they blow out over the Red Sea. Finally, we have found evidence of the upstream cyclonic cell with a core of descending motion during only one other wind event, namely the slightly weaker wind jet that occurred on 7/13 (Davis et al. 2015).

The Tokar Delta is often sighted as a major source of summer dust plumes that can cover significant portions of the Red Sea and Arabian peninsula (Hickey and Goudie 2007). Absent a full aerosol model, there are several 'rules of thumb' that meteorologists commonly use to determine whether conditions are favorable for lofting of dust up into the atmosphere (see www.meted.ucar.edu/mesoprim/dust/print.htm). We now examine those criteria at a site where the core of the wind jet crosses the Tokar Delta region (indicated by a triangle close to the Red Sea shoreline in Fig. 1) over the 24-hour span of extreme wind event (Fig. 17). The first condition is that the ground-level wind speed exceeds 15 knots, which is usually satisfied when the winds at 1000 ft. exceed 30 knots

 doi:10.20944/preprints202009.0738.v1

(about 15 m s^{-1}). It can be seen from Fig. 17 that both conditions are satisfied during all but the afternoon period (13–18 UTC) when the wind relaxes. Bou Karam et al. (2008) describes the lifting of dust at the leading edge of the monsoon flow, a phenomenon that could be relevant during the onset of the TWJ, when the leading edge of the cool and moist monsoon air mass passes down through the Tokar Gap. Although the wind jets in Gaps 2 and 3 achieve near-surface velocities strong enough to lift the fine silt of the Tokar Delta, these gaps do not have comparable delta regions.

Even though the winds may be strong enough to lift dust, unstable stratification is required for the dust to be lofted up to 1000 m. Fig. 17 indicates that the TWJ is capped by stable stratification in the 307–312 K range, roughly from 500 to 1000 m, during its strongest phases (00–10 and 21–24 UTC). However, the region below this transition layer is relatively homogeneous in potential temperature, and statically unstable near ground level, so it is possible that dust could be lofted up to fill a column of 500 m above ground. During the weak phase of the Jet, potential temperature is well mixed up to about 1500 m, but the winds are too weak to lift the dust off the ground. Previously suspended dust within 500 m of ground could be lofted higher during afternoon weak phase by thermal convection. Cuesta et al. (2009) present a similar example over the Sahara.

6. Conclusions

The main thrust of this work has been to describe the anatomy and dynamics of a simulated strong wind event in the Tokar Gap and neighboring gaps, to offer an explanation for the relatively limited downstream reach of the wind jets in the neighboring gaps, and to describe a Lagrangian overview of the circulation associated with the jets. The analysis suggests that the Tokar Wind Jet (TWJ), which spills down through a ravine-like topography, never achieves supercritical speeds and therefore does not undergo a dissipative hydraulic jump as it departs the gap. By contrast, the jets in the neighboring gaps form when air spills down from relatively high passes, resulting in a layer of air that achieves comparable velocities to those of the TWJ but is shallower and therefore more supercritical. These jets do, in fact, experience features resembling hydraulic jumps after they depart the coastline, and become much thicker and weaker downstream of the jump. The model resolution is inadequate to resolve the detailed features of the presumed jumps, but the layer thickness increases, and the horizontal velocity decreases, as air parcels cross it. Downstream of the jump, air parcels turn quickly to the southeast and flow in that general direction, never crossing the Red Sea. The downstream extension of the TWJ easily crosses the Red Sea and reaches the Saudi coast, with some air parcels penetrating across the coastal mountain range and further inland. The horizontal spread of particles, as quantified by the single-particle dispersion tensor, is larger for the Tokar Wind Jet than that for the neighboring gaps. The vertical spread is, on the other hand, slightly larger for the secondary gaps during the first 6 or so hours, plausibly due to the effects of the suspected hydraulic jumps.

 doi:10.20944/preprints202009.0738.v1

The energetics of all the jets, as quantified by transitions in the various terms that constitute the Bernoulli function, suggest the primary exchange is between p/ρ, potential energy, and internal energy, with kinetic energy changes playing a surprisingly secondary role. Diabatic heating along the coast increases the Bernoulli function and makes it difficult to isolate any dissipation of the energy associated with the jumps.

The above scenario has many elements in common with idealized models of ridges with single gaps when the mountain parameter Nh/U is comparable. This includes a gap jet with a long downstream extension, and supercritical flow that spills down from the high-elevation ridge crests and terminates in a hydraulic jump. (Note, however, that idealized models typically do not include secondary gaps.) The lofting of dust into the atmosphere, as observed frequently over the Tokar Delta, is consistent with threshold wind values in our WRF model.

Our simulations have also uncovered at least one phenomenon that appears to be new and is not as easily explained by earlier work. During the onset phase of the 12 July 2008 event, a cyclonic cell with strong descending core flow is generated near the upstream entrance to the Tokar Gap. Many of the air parcel trajectories that enter the Tokar Gap emanate from higher elevation and are carried downward before they veer off horizontally and enter the gap to form a jet. This same cell feeds at least some of the flow into the jets that form gaps to the south of the Tokar Gap. As the jet evolves and eventually weakens, the cyclonic cell moves to the west and out of the high-resolution domain. This sequence of events is observed for the 12 July 2008 as well as a strong event that spans 7/13 (Davis et al. 2015), but it is not observed for any other events

 doi:10.20944/preprints202009.0738.v1

occurring in July and August of that simulating year. Whether strongest events are made so by the presence of the cell, or vice-versa, is a subject that invites further analysis.

Acknowledgements

This study is part of a joint research project by King Abdullah University of Science and Technology (KAUST) and the Woods Hole Oceanographic Institution and was funded by KAUST. Support for Albright was provided by the National Science Foundation under Grant (OCE-0525729). The authors are grateful to Mr. Stephen Maldonado, who assisted with the estimates of the mountain parameter, and to Shannon Davis for some helpful comments.

References

Baines, P. G., 1995: *Topographic Effects in Stratified Flows.* Cambridge U. Press, 482pp.

Bou Karam, D., C. Flamant, P. Knippertz, O. Reitebuch, J. Pelon, M. Chong and A. Dabas 2008. Dust emissions over the Sahel associated with the West African monsoon intertropical discontinuity region: A representative case-study. Q. J. R. Meteorol. Soc. **134**, 6621-634. Doi: 10.1002/qj.244.

Clarke, A. J., 1988: Inertial wind path and sea surface temperature patterns near the Gulf of Tehuantepec and Gulf of Papagayo. *J. Geophys. Res.*, **93,** 15 491–15 501.

Chelton, D. B., M. H. Freilich, and S. K. Esbense, 2000: Satellite observations of the wind jets off the Pacific coast of Central America. Part I: Case studies and statistical characteristics, Mon. Weather Rev., **128**, 1993–2018.

Colle, B. A. and C. F. Mass, 2000: High-resolution observational and numerical simulations of easterly gap flow through the Strait of Juan de Fuca on 9↓10 December 1995 study of the 12 Februrary 1995 event. *Mon. Wea. Rev.*, **128**, 2398–2422.

Davis, S. R., L. J. Pratt and H. Jiang, 2015: The Tokar Gap Jet: Regional Circulation, Diurnal Variability, and Moisture Transport based on Numerical Simulations. *J. Climate*, **28**, 5885–5907.

Farrar, J. T., S. Lentz, J. Churchill, P. Bouchard, J. Smith, J. Kemp, J. Lord, G. Allsup, and D. Hosom, 2009: King Abdullah University of Science and Technology (KAUST) mooring deployment cruise and fieldwork report, Fall 2008, R/V Oceanus Voyage 449-5. Technical report, WHOI-KAUST-CTR-2009-02, Woods Hole Oceanographic Institution and King Abdullah University of Science and Technology, Woods Hole, Massachusetts, USA, 2009. Doi: 10.1575/1912/3012. https://hdl.handle.net/1912/3012

Gabersek and Durran, 2004: Gap flows through idealized topography. Part I: Forcing by large-scale winds in the nonrotating limit. J. Atmos. Sci. **61**, 2846–2862

Gabersek and Durran, 2006: Gap flows through idealized topography. Part II: Effects of rotation and surface Friction. J. Atmos. Sci. **63**, 2720–2739

Gohm, A., G. J. Mayr, A. Fix and A. Giez (2008): On the onset of Bora and formation of rotors and jumps near a mountain gap. *Q. J. R. Meteorol. Soc*. **134**, 21–46.

Hickey, B., and A. S. Goudie, 2007: The use of TOMS and MODIS to identify dust storm source areas: the Tokar delta (Sudan) and the Seistan basin (south west Asia), in *Geomorphological Variations*, edited by A. S. Goudie and J. Kalvoda, pp. 37–57, P3K, Prague.

Jiang, H., J. T. Farrar, R. C. Beardsley, R. Chen and C. Chen 2009: Zonal surface wind jets across the Red Sea due to mountain gap forcing along both sides of the Red Sea. Geophysical Review Letters, **36**, L19605, doi:10.1029/2009GL040008.

Kalenderski, S. and G. Stenchikov 2016: High-resolution regional modeling of summertime transport and impact of African dust over the Red Sea and Arabian Peninsula. J. Geophys. Atmos., **121**, 6435–6458, doi:10.1002/2015JD024480.

Langodan, S., L. Cavaleri, A. Pomaro, Y. Vishwanadhapalli, L. Bertotti and I. Hoteit 2017. The climatology of the Red Sea – part 2: the waves. *International J. of Climatology* **37**, 4518-4528. doi: 10.1002/joc.5101.

Lo, J. C.-F., Z.-L. Yang, and R. A. Pielke Sr., 2008: Assessment of three dynamical climate downscaling methods using the Weather Research and Forecasting (WRF) model, *J. Geophys. Res.*, **113**, D09112, doi:10.1029/2007JD009216.

Magalhaes, J. M., I. B. Araujo, J. C. B. da Silva, R. H. J. Grimshaw, K. Davis, and J. Pineda 2011: Atmospheric gravity waves in the Red Sea: a new hotspot. *Nonlin. Proccesses Geophys*., **18**, 71-79, doi: 10.5194/npg-18-71-2011.

Mayr, G. J, and Coauthors, 2007: Gap flows: results from the Mesoscale Alpine Programme. *Q. J. R. Meteorol. Soc*. **133**, 881–896.

Overland, J. E. 1984: Scale analysis of marine winds in straits and along mountain coasts. *Mon. Wea. Rev.*, **112**, 2530–2534.

Overland J. E. and B. A. Walter 1981: Gap winds in the Juan de Fuca. *Mon. Wea. Rev.* **109**, 2221–2233.

Ogden, K. A. and K. R. Helfrich, 2016: Internal hydraulic jumps in two-layer flows with upstream shear. *J. Fluid Mech.* **789**, 64–92.

Patlakas, P., E. Drakaki, G. Galanis, C. Spyrou and G. Kallos 2017: Wind gust estimation by combining a numerical weather prediction model and statistical post-processing. *Energy Procedia* **125**, 190-198.

Patzert, W. C. 1974: Wind-induced reversal in Red Sea circulation. *Deep-Sea Res.* **21**, 109-121.

Pedgley, D. E., 1974: An outline of the weather and climate of the Red Sea, in *L'Oceanographie Physique de la Mer Rouge*, pp. 9–27, U. N. Ed. Sci. and Cult. Organ., Paris.

Pratt, L. J. and J. A. Whitehead, 2008: *Rotating Hydraulics.* Springer, 589 pp.

Pullen, J., J. D. Doyle, P. May, C. Cavanne, P. Flament, and R. A. Arnone 2008: Monsoon surges trigger oceanic eddy formation and propagation in the lee of the Philippine Islands. *Geophys. Res. Lett.* **35**, L07604, doi:10.1029/2007GL033109.

Reed, T. R., 1931: Gap winds in the Strait of Juan de Fuca. *Mon. Wea. Rev.*, **59**, 373–376.

Rypina, I. I. and L. J. Pratt 2010: Chaotic Advection in an Archipelago. *J. Phys. Oceanogr*. **40**, 1988-2006.

Saito, K. 1993: A numerical study of the local downslope wind “Yamaji-kaze” in Japan. Part 2: Non-linear aspect of the 3-d flow over a mountain with a col. *J. Meteor. Soc. Japan*, **71**, 247↓271.

Skamarock, W. C., and Coauthors, 2008: A description of the advanced research WRF version 3, 113 pp., *NCAR Tech. Note NCAR/TN–475+STR*.

Sharp, J. and and C. F. Mass, 2004: Columbia Gorge gap winds: their climatological influence and synoptic evolution. *Wea. Forecasting*, **19**, 970–992.

Steenburgh, W. J., D. M. Schultz and B. A. Colle, 1998: The structure and evolution of gap outflow over the Gulf of Tehuantepec, Mexico. Mon. Wea. Rev.,**126**, 2673–2691.

Sun, F., and J.-Y. Yu, 2006: Impacts of Central America gap winds on the SST annual cycle in the eastern Pacific warm pool, Geophys. Res. Lett., **33**, L06710, doi:10.1029/2005GL024700.

Sudan Post-Conflict Environmental Assessment Report. Published by the United Nations Environment Programme. 358 pp. 2007. ISBN 978-92-807-2702-9, http://postconflict.unep.ch/sudanreport/sudan_website/index.html

Viste, E., and A. Sorteberg: Moisture transport into the Ethiopian highlands. Int. J. Climatol., 33, 249-263, doi:10.1002/joc.3409.

Zangl, G., 2002: Stratified flow over a mountain with a gap: Linear theory and numerical simulations. *Quart. J. Roy. Meteor. Soc.*, **128**, 927-949.

 doi:10.20944/preprints202009.0738.v1

Zhai, P. and A. Bower 2013: The response of the Red Sea to a strong wind jet near the Tokar Gap in summer. J. Geophys. Res., **118**, DOI: 10.1029/2012JC008444.

Figures

Figure 1. Regional map showing Red Sea Hills, Tokar Gap and Gaps 2 and 3 to the south. 'Tributaries' refer to the north and south entrance channels. The red lines show section locations, and the symbols indicate locations for Hovmöller diagrams, as cited in later figures. Topographic elevation contours are labeled in meters.

Figure 2. MODIS image taken at 8:00 UTC on 7/11/2002 showing dust plume associated with northwestward flow through the Tokar Gap and other gaps in the neighboring Red Sea Hills. (Courtesy of NASA: see http://visibleearth.nasa.gov.)

Figure 3. Mean 10m wind vectors and sea level pressure (blue contours) for July 2008, from WRF model. The terrain height is shown in grey.

Figure 4. Hovmöller diagrams for the 7/12/2008 event. Shown are along-thalweg component of horizontal velocity vs. time and elevation at (a): the head of the northern spillway; (b): in the narrowest portion of the gap; and (c): out over the Red Sea. The locations of the stations are indicated by stars in Fig. 1, with (a) lying close to point *a'*,

 doi:10.20944/preprints202009.0738.v1

(b) lying just northeast of *D*, and (c) lying near *E*. Although (b) is taken well downstream of (a), the ground elevations of the two stations are similar, a consequence of the banking of the jet core at (b) up against the canyon sidewall. Time is UTC (local Saudi time minus 3 hours).

Figure 5. Longitudinal sections of potential temperature and the along-section velocity component beginning in eastern (top) and western (bottom) spillways. The orientation of the section line is constant within each panel but changes between panels: thus the along-section velocity component is discontinuous. The data is plotted at 05 UTC on 12/7/2008 and section locations are shown in Fig. 1.

Figure 6. Horizontal wind speed and potential temperature along the path FG of the down-slope flow through Gap 2 (indicated on Fig. 1) at 05 UTC on 7/12/2008.

Figure 7. Cross sections of normal velocity and potential temperature, beginning upstream and proceeding down through the Tokar Gap and out over the Red Sea. The viewer faces downstream (roughly eastward). The data is plotted at 05 UTC (8 AM local time) on 7/12/2008. Section locations are shown in Fig. 1.

Figure 8. Plan views of 10 m wind speed (a) and ground-level potential temperature (b) at 05 UTC on 7/12/2008. Velocity arrows at 10 m are shown in both frames.

 doi:10.20944/preprints202009.0738.v1

Figure 9. WRF profiles of component of wind towards NE (left) and buoyancy frequency (right) taken at three stations upstream of the Tokar Gap at 7/12/2008 at 00 UTC. The station locations are indicated by the color boxes in the inset at the lower left. The z=2500m level, which roughly corresponds to the elevation of the highest peak in the Red Sea Hills, is indicated by a horizontal dashed line (one for each station.) The small inset profiles show the wind speed and N over the full elevation range of the model, both in z and in pressure.

Figure 10 (a): Thickness of the layer formed between ground level and the 312 K surface. (b): The local Froude number F_d based on the 1.5-layer model with interface at 312 K. Both plots for 05 UTC on 7/12/2008.

Figure 11. Forward time (black) and backward time (red) trajectories, initiated at the time indicated on each frame and within a horizontal patch (blue area) lying z=100m and where the wind speed exceeds 15m/s. Trajectories are integrated backward to 12UTC on 7/11/08 and forward in time to 24 UTC on 7/12/08.

Figure 12. Similar to Fig. 11, but now the viewer faces SE and the trajectories are initiated at the four levels z=100, 500, 1000 and 1500m and where the wind speed exceeds 15m/s. Forward/backward trajectories are color-coded blue-to-

 doi:10.20944/preprints202009.0738.v1

green/magenta-to-yellow according to their release height (i.e., blue/magenta at 100m and green/yellow at 1500m).

Figure 13. Similar to Fig. 11, but the trajectories are released at z=500 m in the outflows of the Gap 2 (the gap immediately to the south of the TG) over an area where the wind speed exceeds 15m/s. Frame e (below) is enlarged and slightly rotated version of Frame c.

Figure 13e. A zoomed-in and rotated view of Frame c of Fig. 13. (See caption for Fig. 13, above).

Figure 14. Trajectories initiated within the cyclonic cell at z=1000m (Frames a-c) and 1500m (Frames d-e) at the times indicated and over areas where the downward vertical velocity, *w,* exceeds the value 0.25m/s.

Figure 15. The Bernoulli function (a) and its constituents (b-e) as functions of time (UTC) following the four trajectories plotted (f). The pink/green trajectory passes through the Tokar Gap while the three red/black trajectories pass through the gap immediately to the south. The trajectories are initiated at the (blue) transition point and integrated back and forward in time. Frame (g) shows potential temperature along the four trajectories.

 doi:10.20944/preprints202009.0738.v1

Figure 16. Single-particle dispersion (D) in the horizontal (D_τ, D_n) and vertical (D_z) direction calculated for groups of trajectories initiated at the exits of the Tokar Gap (left) and Gap 2 (right). 25 trajectories were released every hour from 00 UTC to 09 UTC on 07/12/2008. Dispersion curves for the individual releases are shown in grey, and means are shown by thick colored curves, dashed for the Tokar Gap and solid for Gap 2. Dashed curves are superimposed in the right panels for comparison purposes. In each case the trajectories were initiated at z=500 m, and where the horizontal wind speed exceeds 10 ms^{-1}.

Figure 17. Hovmöller diagram for potential temperature and horizontal wind speed as a function of elevation over 7/12/08. The data comes from a location over the Tokar Delta, indicated by a triangle in Fig. 1.

Preprints (www.preprints.org) | NOT PEER-REVIEWED | Posted: 30 September 2020 doi:10.20944/preprints202009.0738.v1

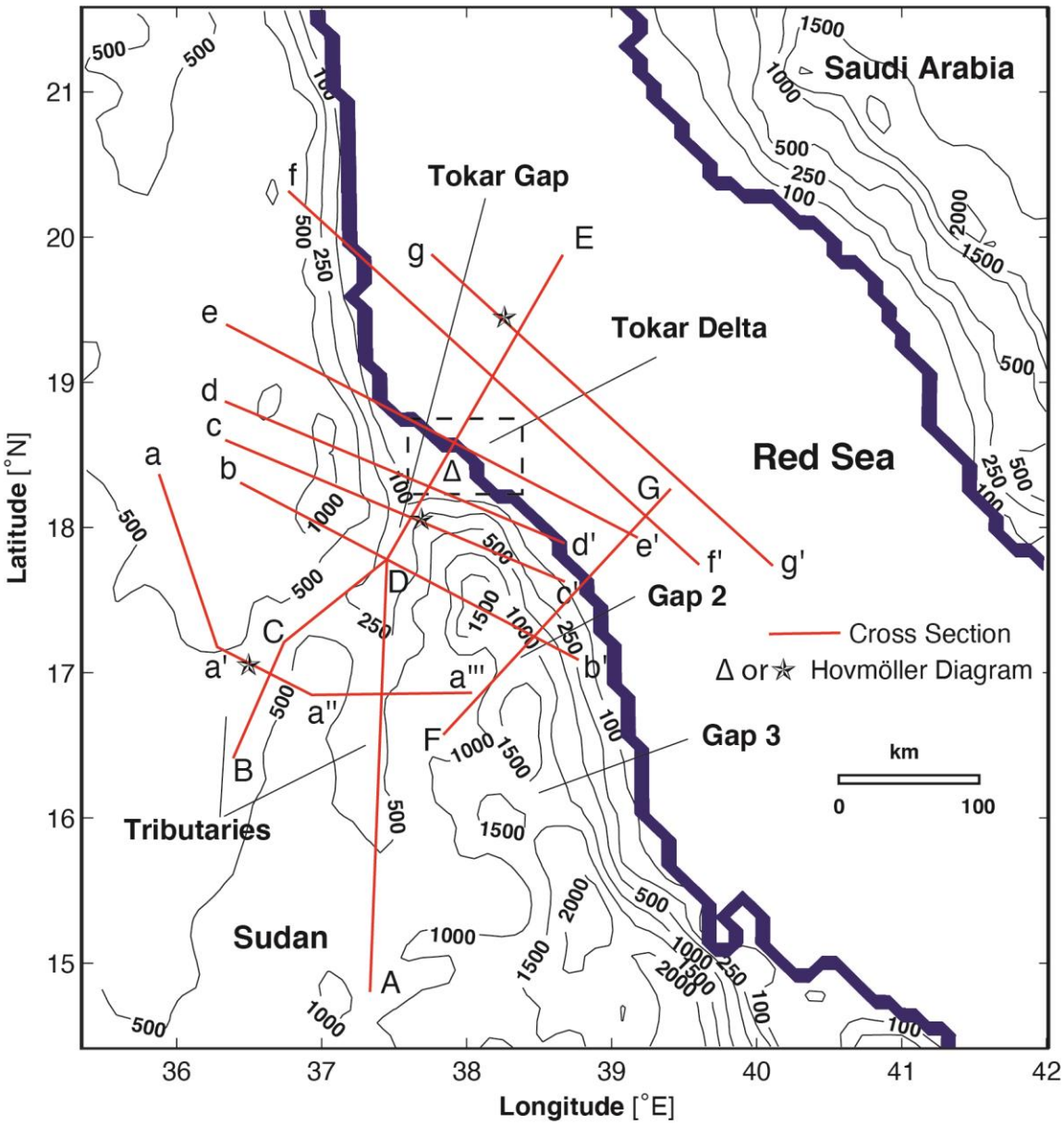

Figure 1. Regional map showing Red Sea Hills, Tokar Gap and Gaps 2 and 3 to the south. 'Tributaries' refer to the north and south entrance channels. The red lines show section locations, and the symbols indicate locations for Hovmöller diagrams, as cited in later figures. Topographic elevation contours in meters.

 doi:10.20944/preprints202009.0738.v1

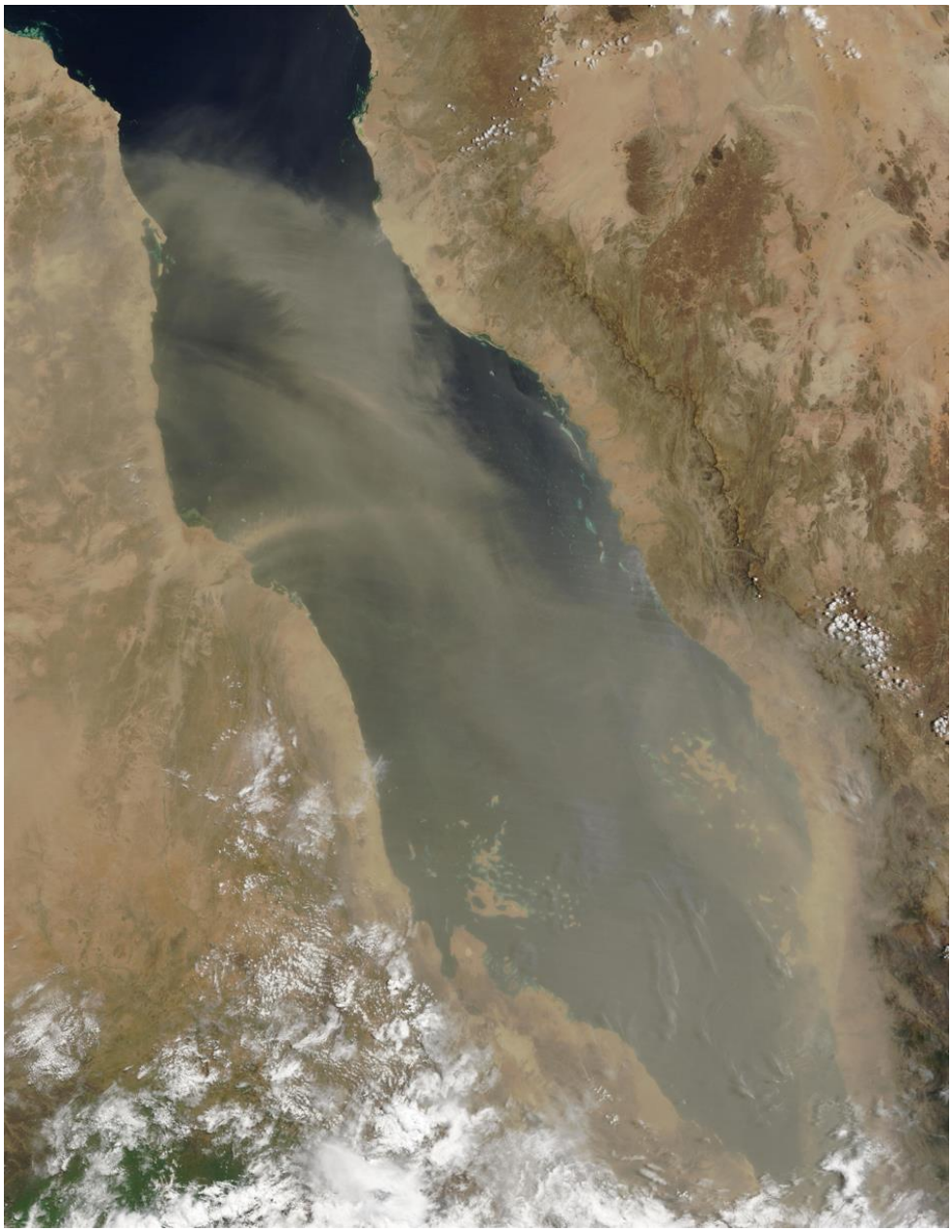

Figure 2. MODIS image taken at 08 UTC on 7/11/2002 showing dust plume associated with northwestward flow through the Tokar Gap and other gaps in the neighboring Red Sea Hills. (Courtesy of NASA: see http://visibleearth.nasa.gov.)

Preprints (www.preprints.org) | NOT PEER-REVIEWED | Posted: 30 September 2020 doi:10.20944/preprints202009.0738.v1

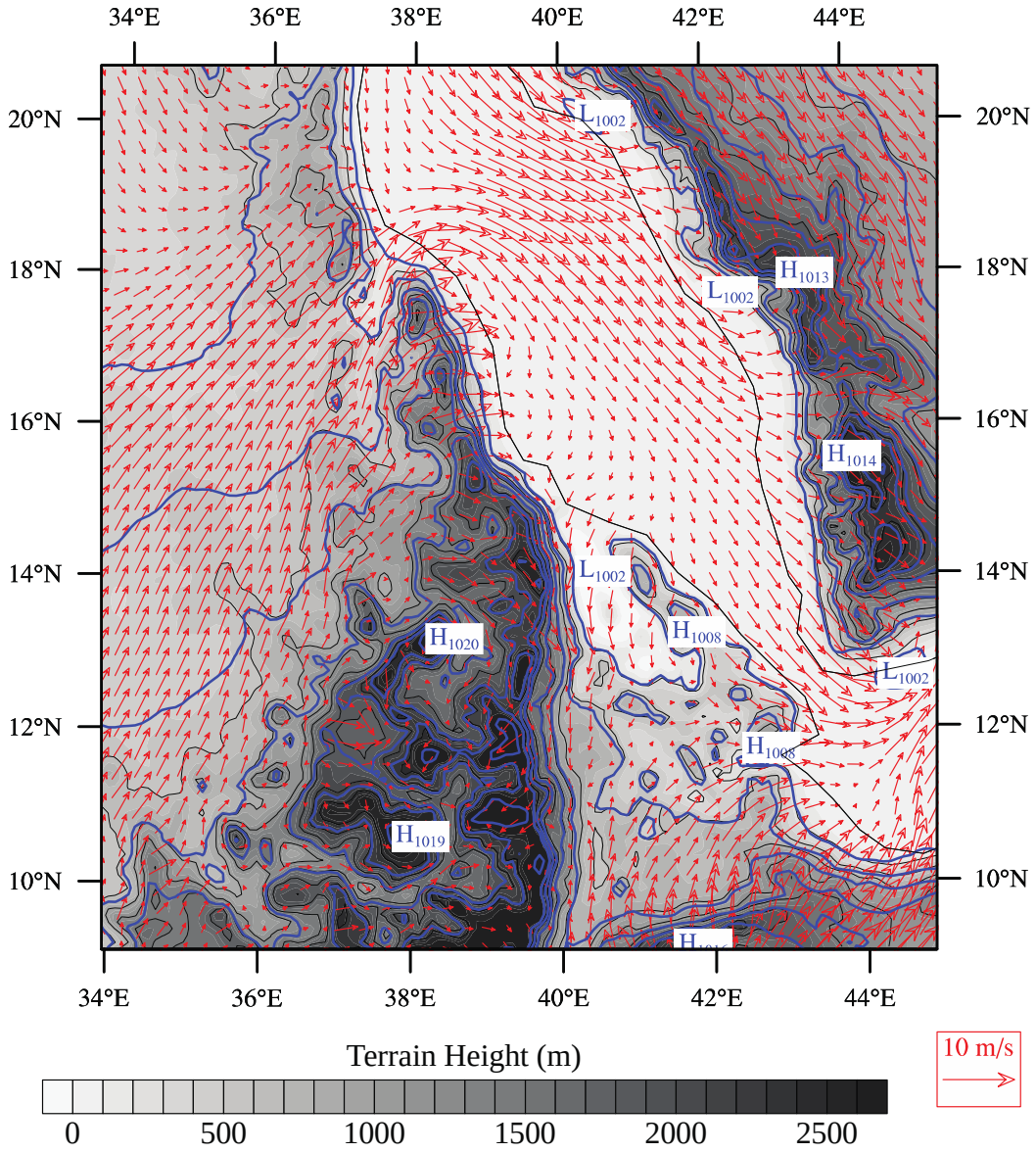

Figure 3. Mean 10 m wind vectors and sea level pressure for July 2008, from WRF model.

Preprints (www.preprints.org) | NOT PEER-REVIEWED | Posted: 30 September 2020 doi:10.20944/preprints202009.0738.v1

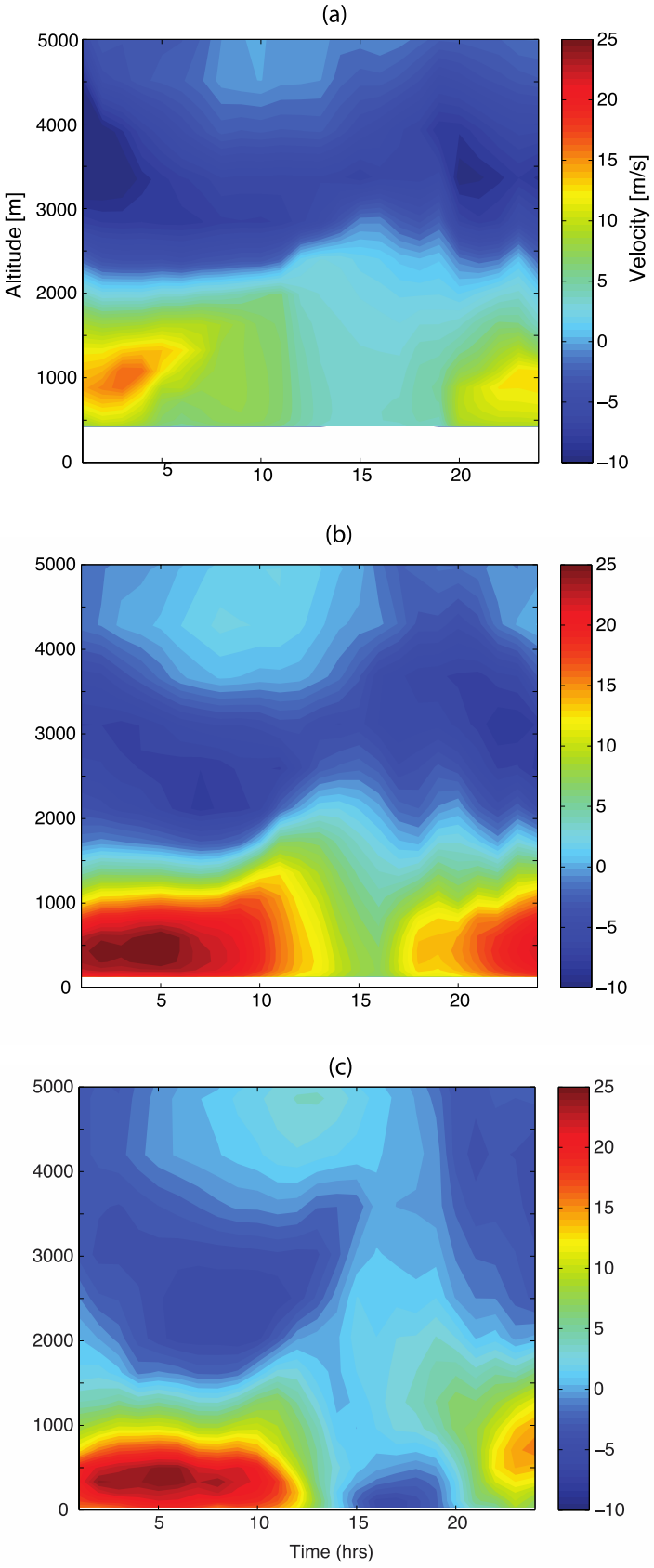

 doi:10.20944/preprints202009.0738.v1

Figure 4. Hovmöller diagrams for the 7/12/08 event. Shown are along-thalweg component of horizontal velocity vs. time and elevation at (a): the head of the northern spillway; (b): in the narrowest portion of the gap; and (c): out over the Red Sea. The locations of the stations are indicated by stars in Figure 1, with (a) lying close to point *a′*, (b) lying just northeast of *D*, and (c) lying near *E*. Although (b) is taken well downstream of (a), the ground elevations of the two stations are similar, a consequence of the banking of the jet core at (b) up against the canyon sidewall. Time is UTC (local Saudi time minus 3 hours).

Preprints (www.preprints.org) | NOT PEER-REVIEWED | Posted: 30 September 2020 doi:10.20944/preprints202009.0738.v1

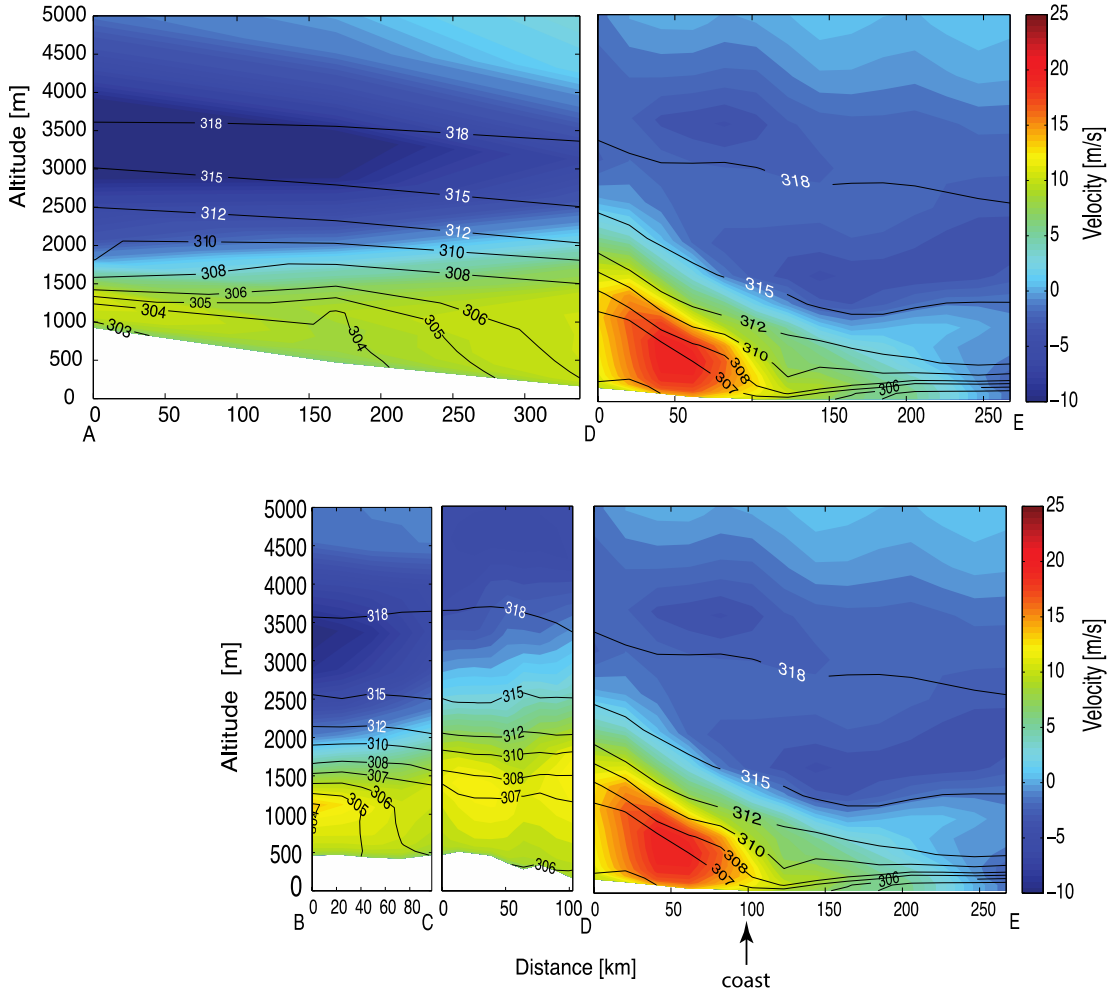

Figure 5. Longitudinal sections of potential temperature and the along-section velocity component beginning in eastern (top) and western (bottom) spillways. The orientation of the section line is constant within each panel but changes between panels: thus the along-section velocity component is discontinuous. The data is plotted at 05 UTC on 7/12/08 and section locations are shown in Figure 1.

Preprints (www.preprints.org) | NOT PEER-REVIEWED | Posted: 30 September 2020 doi:10.20944/preprints202009.0738.v1

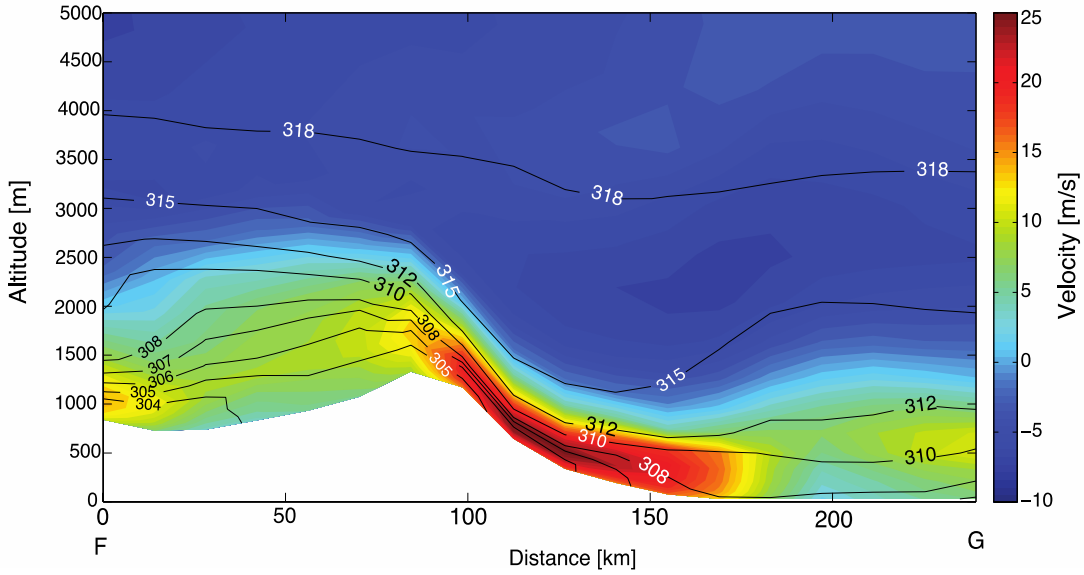

Figure 6. Horizontal wind speed and potential temperature along the path FG of the down-slope flow through Gap 2 (indicated on Fig. 1) at 05 UTC on 7/12/08.

Preprints (www.preprints.org) | NOT PEER-REVIEWED | Posted: 30 September 2020 doi:10.20944/preprints202009.0738.v1

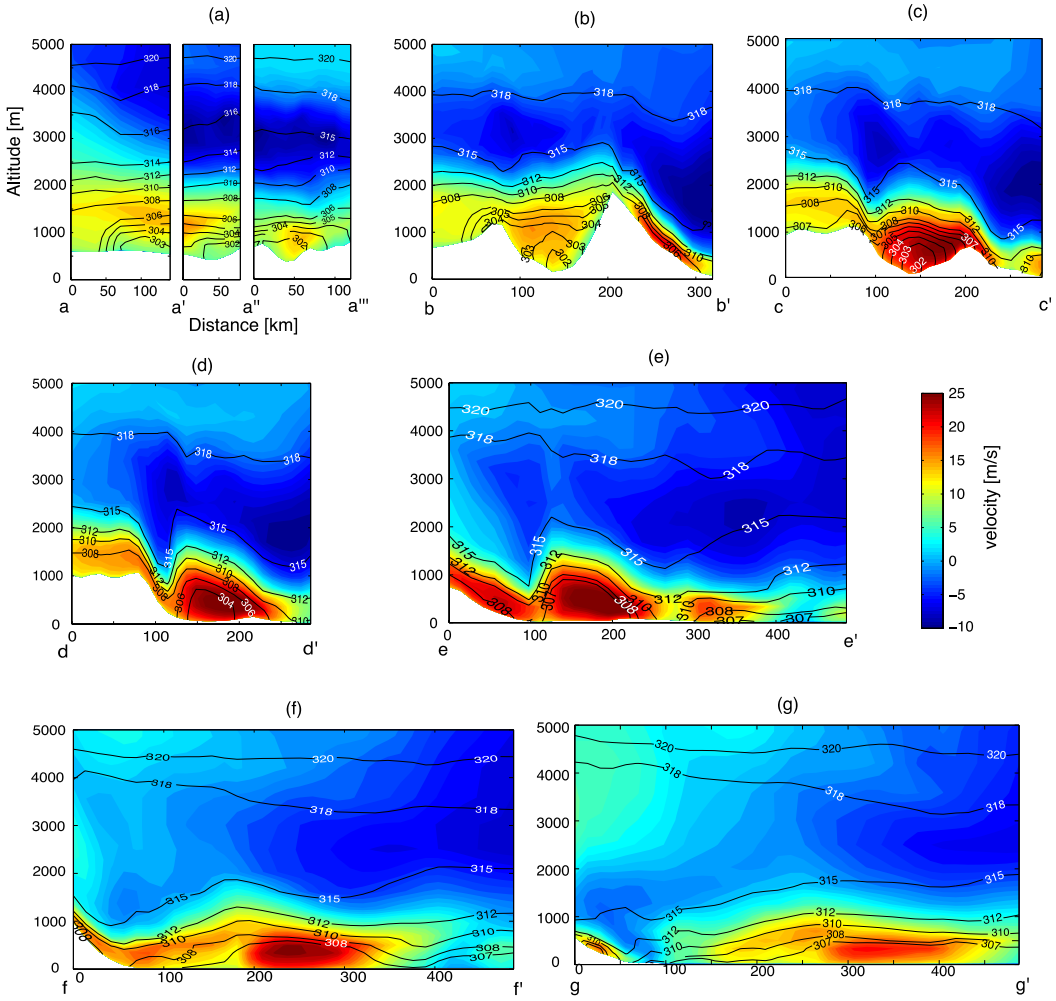

Figure 7. Cross sections of normal velocity and potential temperature, beginning upstream and proceeding down through the Tokar Gap and out over the Red Sea. The viewer faces downstream (roughly eastward). The data is plotted at 05 UTC (8 AM local time) on 7/12/2008. Section locations are shown in Fig. 1.

Preprints (www.preprints.org) | NOT PEER-REVIEWED | Posted: 30 September 2020 doi:10.20944/preprints202009.0738.v1

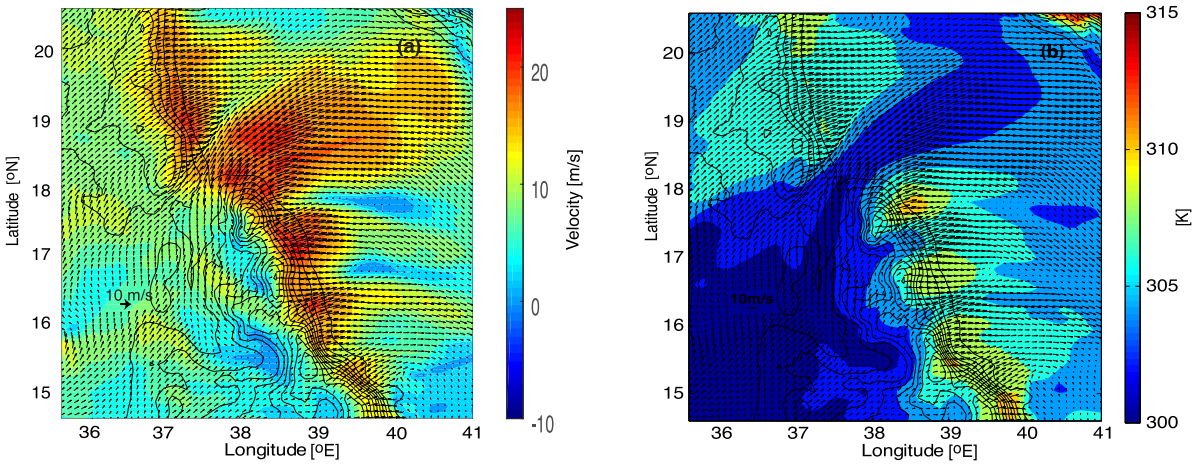

Figure 8. Plan views of 10 m wind speed (a) and ground-level potential temperature (b) at 05 UTC on 7/12/08. Velocity arrows at 10 m are shown in both frames.

Preprints (www.preprints.org) | NOT PEER-REVIEWED | Posted: 30 September 2020 doi:10.20944/preprints202009.0738.v1

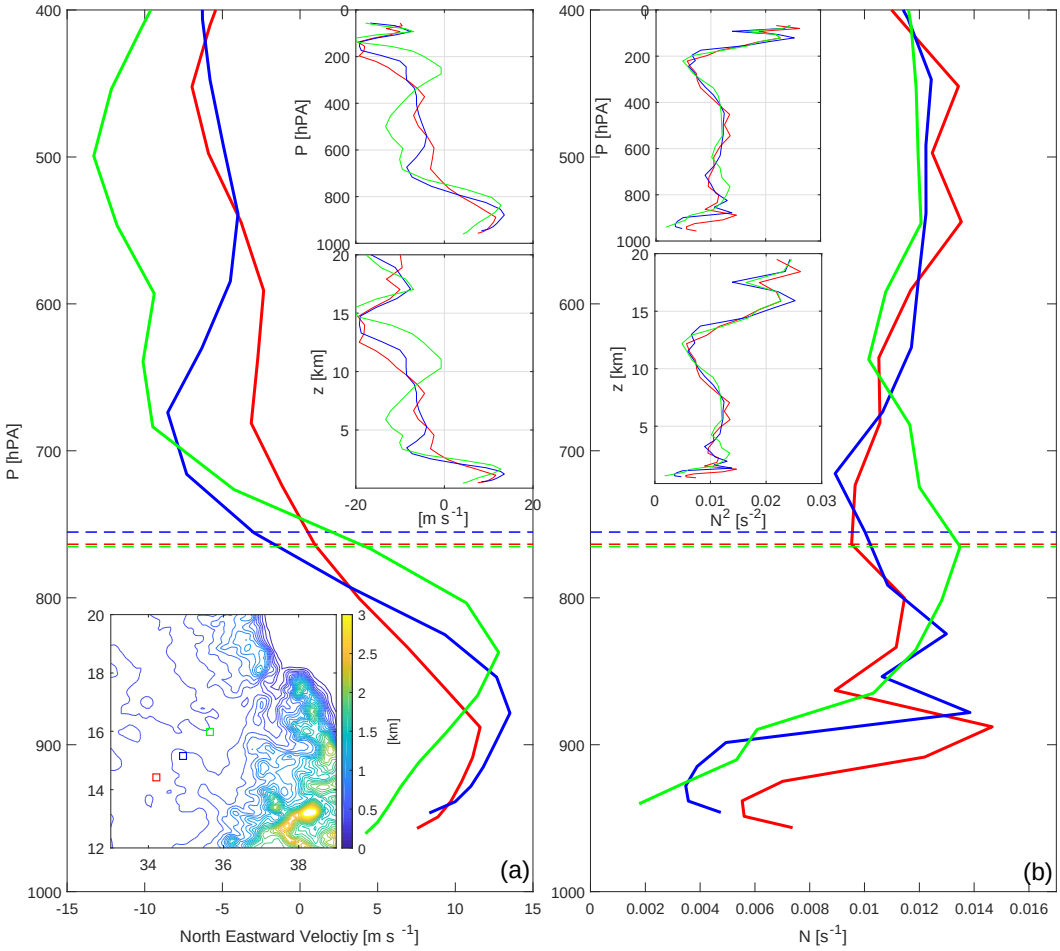

Figure 9. WRF profiles of component of wind towards NE (left) and buoyancy frequency (right) taken at three stations upstream of the Tokar Gap at 7/12/2008 at 00 UTC. The station locations are indicated by the color boxes in the inset at the lower left. The z=2500m level, which roughly corresponds to the elevation of the highest peak in the Red Sea Hills, is indicated by a horizontal dashed line (one for each station.) The small inset profiles show the wind speed and *N* over the full elevation range of the model, both in *z* and in pressure.

Preprints (www.preprints.org) | NOT PEER-REVIEWED | Posted: 30 September 2020 doi:10.20944/preprints202009.0738.v1

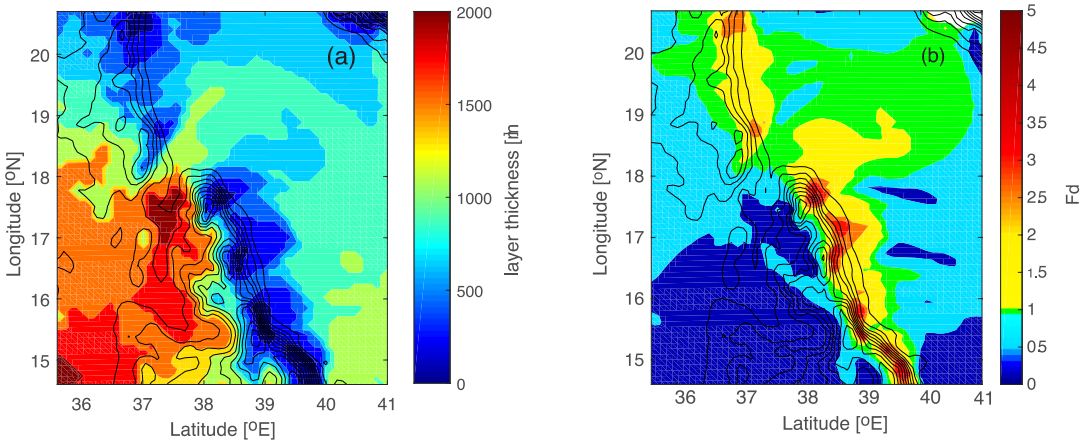

Figure 10 (a): Thickness of the layer formed between ground level and the 312 K surface. (b): The local Froude number F_d based on the 1.5-layer model with interface at 312 K. Both plots for 05 UTC on 7/12/2008.

Preprints (www.preprints.org) | NOT PEER-REVIEWED | Posted: 30 September 2020 doi:10.20944/preprints202009.0738.v1

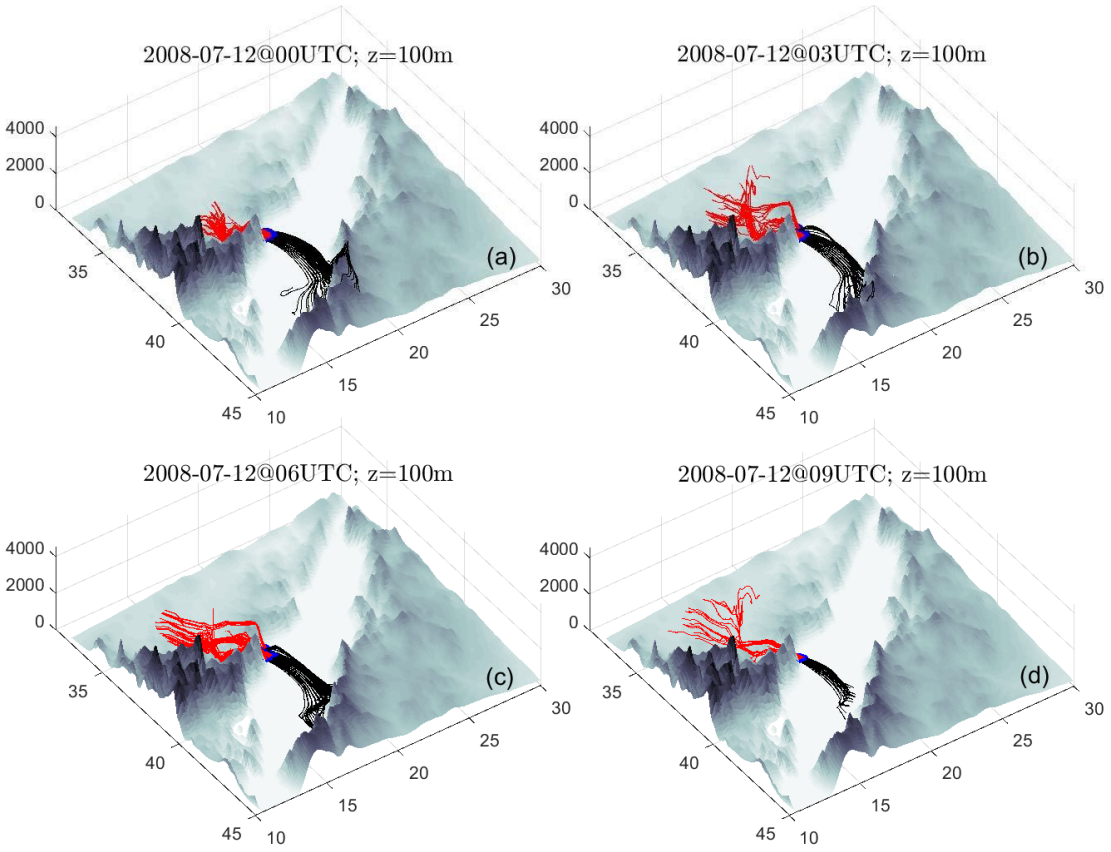

Figure 11. Forward time (black) and backward time (red) trajectories, initiated at the time indicated on each frame and within a horizontal patch (blue area) lying z=100m and where the wind speed exceeds 15m/s. Trajectories are integrated backward to 12UTC on 7/11/08 and forward in time to 24 UTC on 7/12/08.

Preprints (www.preprints.org) | NOT PEER-REVIEWED | Posted: 30 September 2020 doi:10.20944/preprints202009.0738.v1

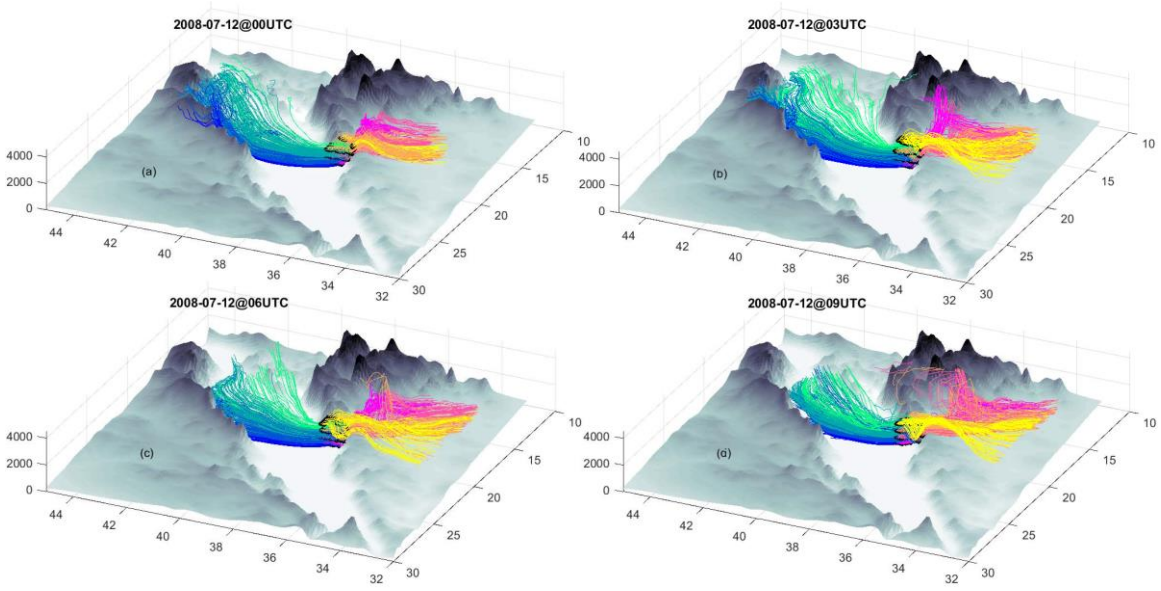

Figure 12. Similar to Figure 11, but now the viewer faces SE and the trajectories are initiated at the four levels z=100, 500, 1000 and 1500 m and where the wind speed exceeds 15 m/s. Forward/backward trajectories are color-coded blue-to-green/magenta-to-yellow according to their increasing release height (i.e., blue/magenta at 100 m and green/yellow at 1500 m).

Preprints (www.preprints.org) | NOT PEER-REVIEWED | Posted: 30 September 2020 doi:10.20944/preprints202009.0738.v1

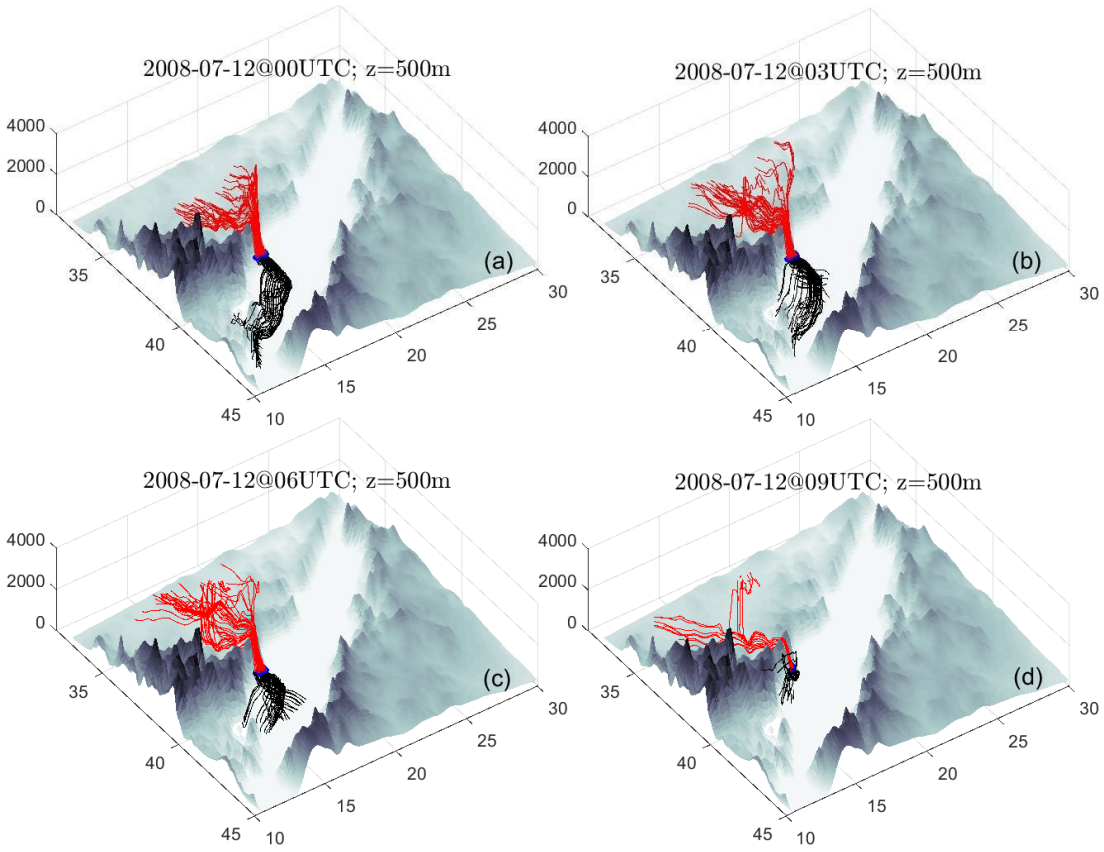

Figure 13. Similar to Fig. 11, but the trajectories are released at z=500 m in the outflows of the Gap 2 (the gap immediately to the south of the TG) over an area where the wind speed exceeds 15m/s. Frame e (below) is enlarged and slightly rotated version of Frame c.

Preprints (www.preprints.org) | NOT PEER-REVIEWED | Posted: 30 September 2020 doi:10.20944/preprints202009.0738.v1

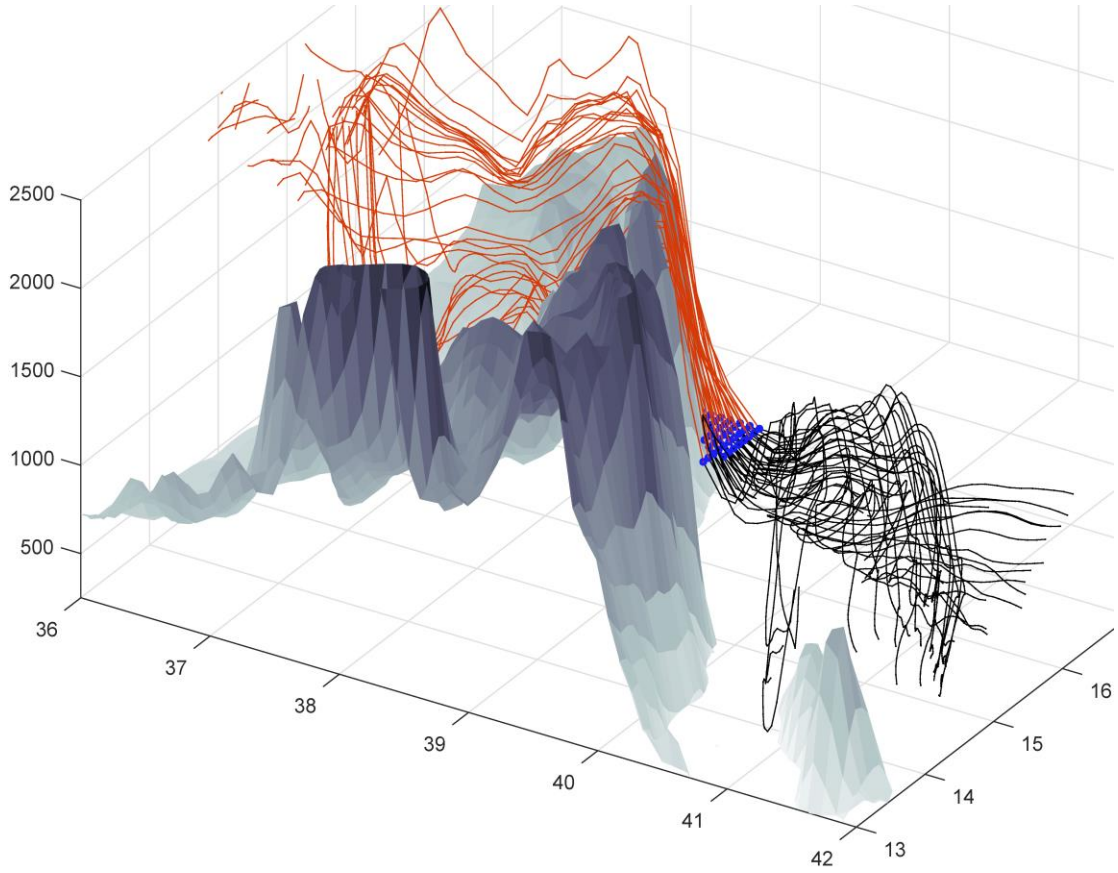

Figure 13e. A zoomed-in and rotated view of Frame c of Fig. 13. (See caption for Fig. 13, above).

Preprints (www.preprints.org) | NOT PEER-REVIEWED | Posted: 30 September 2020 doi:10.20944/preprints202009.0738.v1

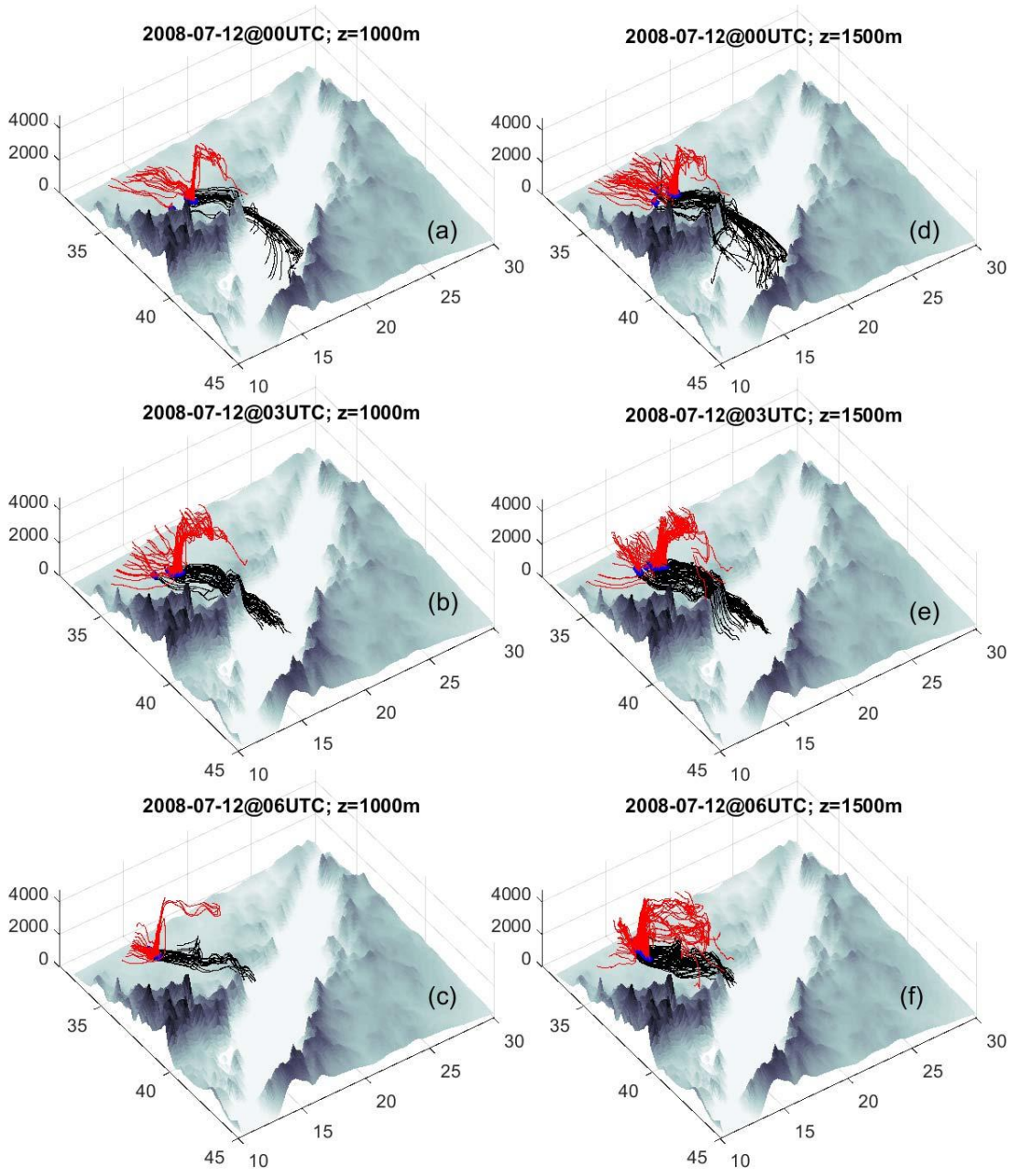

Figure 14. Trajectories initiated within the cyclonic cell at z=1000m (Frames a-c) and 1500m (Frames d-e) at the times indicated and over areas where the downward vertical velocity, *w,* exceeds the value 0.25m/s.

Preprints (www.preprints.org) | NOT PEER-REVIEWED | Posted: 30 September 2020 doi:10.20944/preprints202009.0738.v1

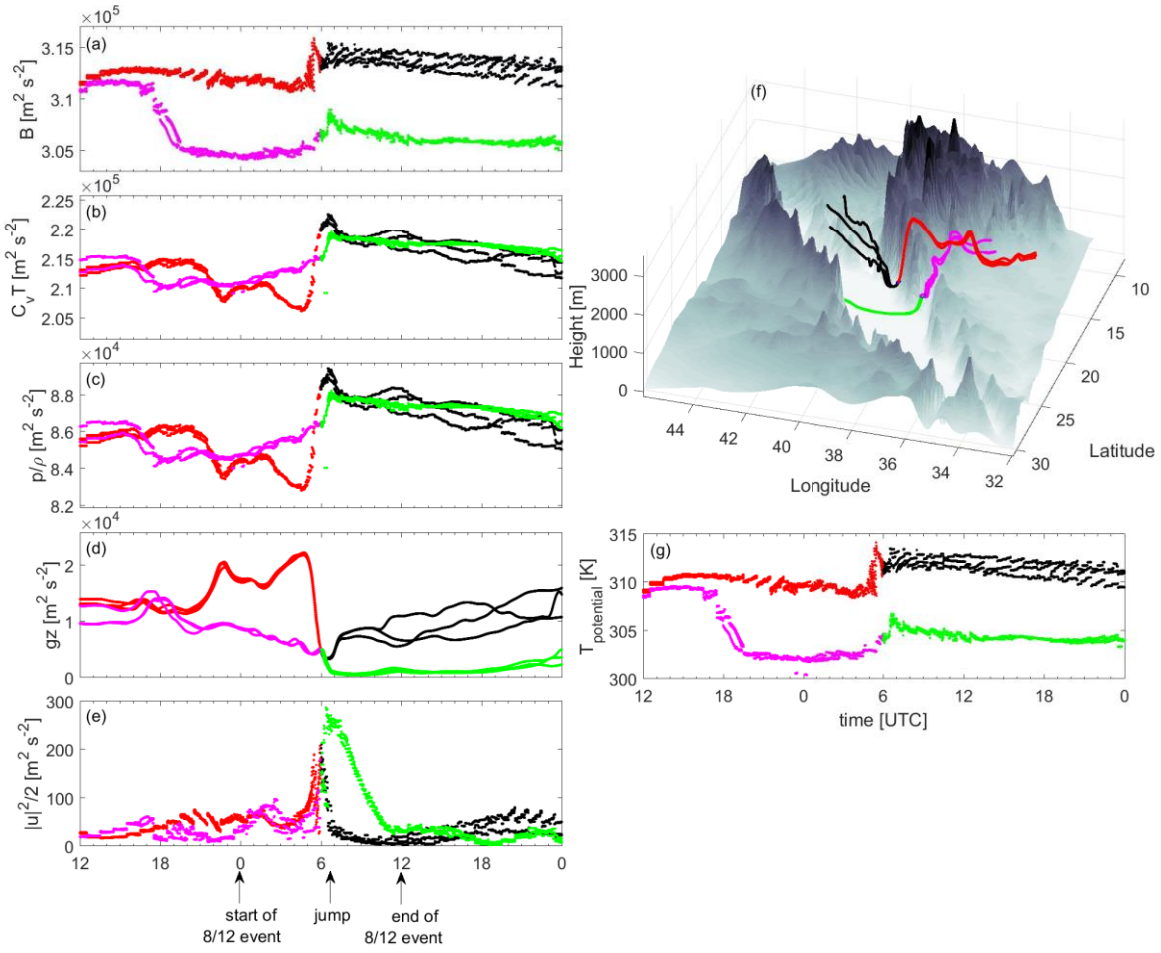

Figure 15. The Bernoulli function (a) and its constituents (b-e) as functions of time (UTC) following the four trajectories plotted (f). The pink/green trajectory passes through the Tokar Gap while the three red/black trajectories pass through the gap immediately to the south. The trajectories are initiated at the (blue) transition point and integrated back and forward in time. Frame (g) shows potential temperature along the four trajectories.

Preprints (www.preprints.org) | NOT PEER-REVIEWED | Posted: 30 September 2020 doi:10.20944/preprints202009.0738.v1

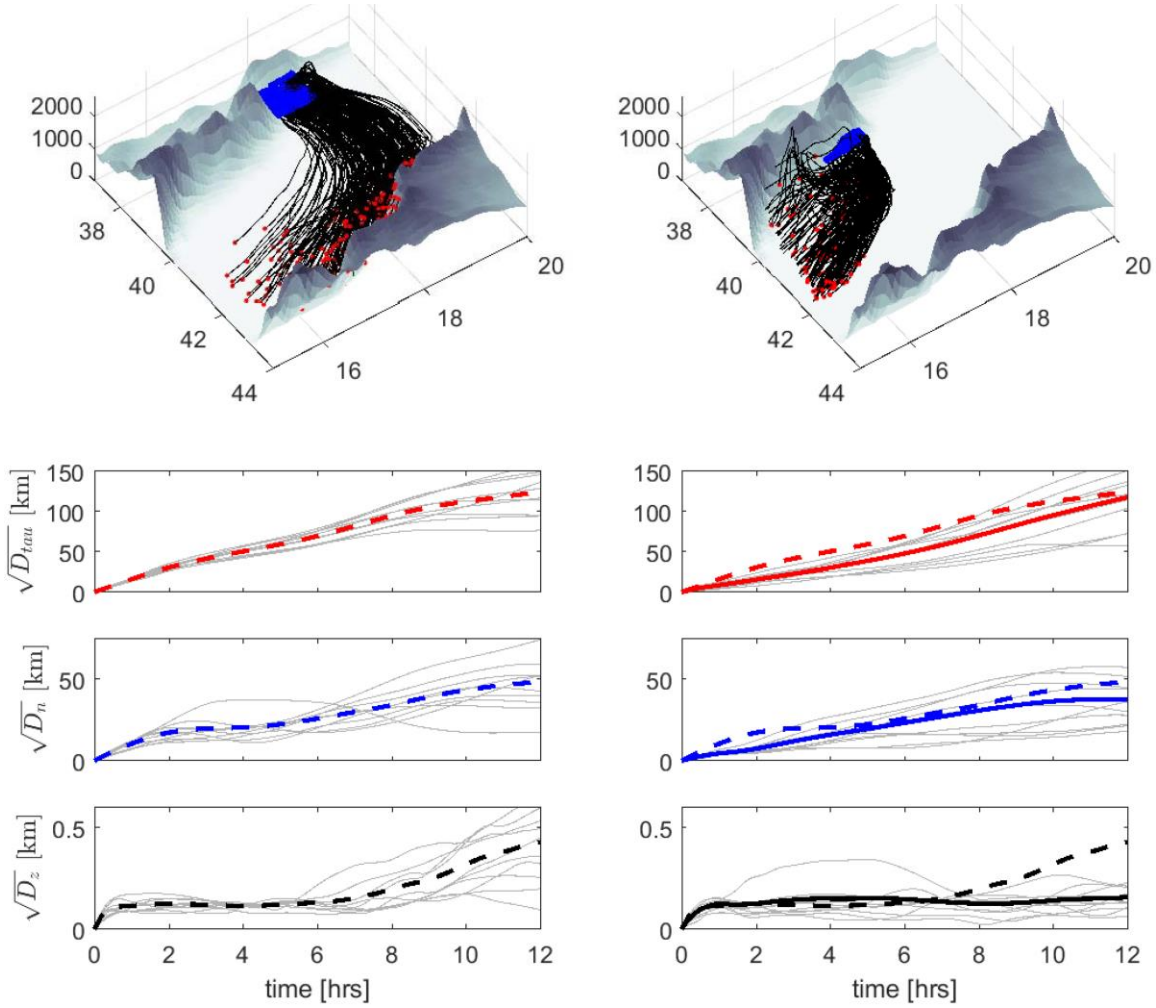

Figure 16. Single-particle dispersion (D) in the horizontal ($\overline{D_\tau}$, $\overline{D_n}$) and vertical ($\overline{D_z}$) direction calculated for groups of trajectories initiated at the exits of the Tokar Gap (left) and Gap 2 (right). 25 trajectories were released every hour from 00 UTC to 09 UTC on 07/12/2008. Dispersion curves for the individual releases are shown in grey, and means are shown by thick colored curves, dashed for the Tokar Gap and solid for Gap 2. Dashed curves are superimposed in the right panels for comparison purposes. In each case the trajectories were initiated at z=500 m, and where the horizontal wind speed exceeds 10 ms^{-1}.

Preprints (www.preprints.org) | NOT PEER-REVIEWED | Posted: 30 September 2020 doi:10.20944/preprints202009.0738.v1

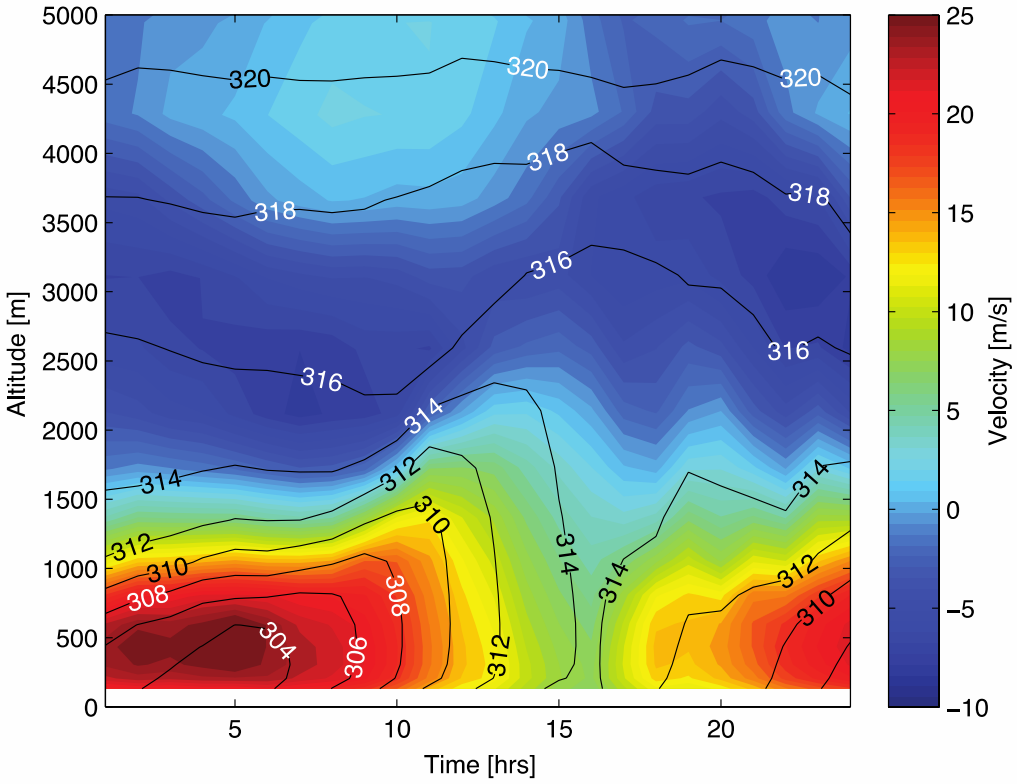

Figure 17. Hovmöller diagram for potential temperature and horizontal wind speed as a function of elevation over 7/12/08. The data comes from a location over the Tokar Delta, indicated by a triangle in Fig. 1.